

# Magnetic flux closure in mutant magnetotactic bacteria elucidates a key signature of magnetofossils

**Matthieu Amor**

Aix-Marseilles University/CNRS <https://orcid.org/0000-0002-4299-1493>

**Juan Wan**

University of California, Berkeley

**Ramon Egli**

Central Institute for Meteorology and Geodynamics <https://orcid.org/0000-0001-6825-4742>

**Julie Carlut**

Université de Paris

**Christophe Gatel**

CEMES

**Ingrid Marie Andersen**

Centre d'Élaboration de Matériaux et d'Etudes Structurales

**Etienne Snoeck**

Centre d'Élaboration de Matériaux et d'Etudes Structurales

**Arash Komeili** (✉ [komeili@berkeley.edu](mailto:komeili@berkeley.edu))

University of California, Berkeley

---

## Article

**Keywords:** Biomineralization, Magnetofossils, Vortex State, First-Order Reversal Curves, Electron Holography

**Posted Date:** February 12th, 2021

**DOI:** <https://doi.org/10.21203/rs.3.rs-187824/v1>

**License:** © ⓘ This work is licensed under a Creative Commons Attribution 4.0 International License.

[Read Full License](#)

---

1           **Magnetic flux closure in mutant magnetotactic bacteria**  
2                   **elucidates a key signature of magnetofossils**

3   Matthieu Amor<sup>a,b\*</sup>, Juan Wan<sup>a\*</sup>, Ramon Egli<sup>c,d\*</sup>, Julie Carlut<sup>a</sup>, Christophe Gatel,<sup>e,f</sup> Ingrid Marie  
4                   Andersen<sup>e</sup>, Etienne Snoeck<sup>e</sup>, Arash Komeili<sup>a,g</sup>

5       <sup>a</sup>Department of Plant and Microbial Biology, University of California, Berkeley, CA  
6                   94720-3102

7       <sup>b</sup>Aix-Marseille University, CNRS, CEA, UMR7265 Biosciences and Biotechnology  
8       Institute of Aix-Marseille, CEA Cadarache, Saint-Paul-lez-Durance, F-13108, France

9       <sup>c</sup>Zentralanstalt für Meteorologie und Geodynamik (ZAMG), Hohe Warte 38, A-1190  
10                   Vienna, Austria

11       <sup>d</sup>Université de Paris, Institut de Physique du Globe de Paris, CNRS, 75005 Paris, France

12                   <sup>e</sup>CEMES CNRS, 29 rue Jeanne Marvig, F-31055 Toulouse, France

13                   <sup>f</sup>Université de Toulouse, F-31077 Toulouse, France

14       <sup>g</sup>Department of Molecular and Cell Biology, University of California, Berkeley, CA  
15                   94720-3200

16                   MA, JW and RE contributed equally to this work.

17                   Corresponding authors:

18       [matthieu.amor@cea.fr](mailto:matthieu.amor@cea.fr) (MA); [ramon.egli@zamg.ac.at](mailto:ramon.egli@zamg.ac.at) (RE); [komeili@berkeley.edu](mailto:komeili@berkeley.edu) (AK)

19

20   Keywords: Biomineralization, Magnetofossils, Vortex State, First-Order Reversal  
21   Curves, Electron Holography

## 22 **Abstract**

23 Magnetotactic bacteria (MTB) produce single- or multi-stranded chains of magnetic  
24 nanoparticles that contribute to the magnetization of sedimentary rocks. Their magnetic  
25 fingerprint can be detected in ancient geological samples, and serve as a unique  
26 biosignature of microbial life. However, fossilized assemblages bear contradictory  
27 signatures pointing to magnetic components that have distinct origin(s). Here, we produce  
28 mutant bacteria to mimic MTB producing multi-stranded chains that cannot be cultivated  
29 in the laboratory, and show that the unresolved magnetic signatures are fully compatible  
30 with the contribution of MTB synthesizing multi-stranded nanoparticle chains and with  
31 fold-collapsed single-stranded chains. These structures generate magnetic flux-closing  
32 configurations while maintaining high remanent magnetizations. This work has important  
33 paleoclimatic, paleontological and phylogenetic implications, as it provides a novel tool to  
34 differentiate distinct MTB lineages (single- vs multi-stranded nanoparticle chains) which  
35 will enable the tracking of the evolution of some of the most ancient biomineralizing  
36 organisms in a time-resolved manner.

37

38

### 39 Introduction

40 Magnetite ( $\text{Fe}_3\text{O}_4$ ) is a ubiquitous iron oxide found in sediments and in many sedi-  
41 mentary rocks. It is a major carrier of sediment and rock magnetization used for numerous  
42 applications in Earth sciences including paleomagnetic, paleoclimate, paleoenvironmental,  
43 paleogeographic and paleontological reconstructions <sup>1</sup>. In addition to lithogenic crystals,  
44 secondary magnetite particles form in sediments through chemical and diagenetic  
45 processes, but can also be produced by bacteria <sup>2</sup>.

46 Magnetotactic bacteria (MTB) are the only known microorganisms producing  
47 intracellular nanoparticles of magnetite in organelles called magnetosomes under a  
48 genetically controlled pathway <sup>3</sup>. They represent some of the most ancient biomineralizing  
49 organisms, with a proposed origin of  $\sim 3$  Ga <sup>4</sup>. They are markers of oxic-anoxic transition  
50 zones in aquatic and sedimentary environments <sup>5,6</sup>, making them useful paleoenvironmental  
51 indicators <sup>7-9</sup>. Magnetosomes are assembled in chains, and provide the bacteria with a  
52 magnetic dipole for navigation purposes <sup>10</sup>. When MTB cells die, their magnetite chains can  
53 be trapped into sediments and subsequently fossilized <sup>11,12</sup>. MTB fossils (hereafter referred  
54 to as magnetofossils) can be preserved over geological times and contribute to sedimentary  
55 paleomagnetic and environmental records <sup>13,14</sup>. Their unambiguous identification, and  
56 discrimination from abiotic magnetite, would thus provide strong constraints on the  
57 evolution of life, biomineralization processes, and environmental conditions over  
58 geological times.

59 First-order reversal curve (FORC) diagrams, which rely on the measurement of partial  
60 hysteresis curves, can be used to discriminate isolated single-domain (SD) magnetite  
61 particles and magnetofossils from other magnetic structures, such as SD particle clusters

62 and larger lithogenic (titano)magnetite crystals containing magnetic vortices (VO) or mul-  
63 tiple magnetic domains (MD) <sup>15,16</sup>, through a sharp signature called the central ridge <sup>17,18</sup>, down  
64 to concentrations inaccessible with other characterization methods. Principal component  
65 analyses (PCA) of FORC diagrams obtained from magnetofossil-rich sediments typically  
66 yield mixtures of MD and VO signatures with a large vertical dispersion around the SD-  
67 related central ridge that contribute to 40-65% of the total magnetization (Table 1) <sup>19</sup>. These  
68 results can be explained by mixtures of (i) well-dispersed non-interacting SD particles or  
69 linear chains of such particles contributing to the central ridge, and (ii) clumped SD and/or  
70 VO particles contributing to the remaining parts of the FORC distribution. The associated  
71 magnetic hysteresis parameters (see glossary in the SI appendix) describing the shape of  
72 the hysteresis loop are close to the theoretical limit for non-interacting SD particles and  
73 magnetosome chains (Table 1). In particular, the hysteresis squareness (the ratio of  
74 remanent and saturation magnetizations) of ~0.45 is unrealistically large for samples  
75 containing strongly interacting SD particles or VO particles associable with the observed  
76 FORC contributions around the central ridge <sup>20-22</sup>(Fig. 1). Collapsed obtained from MTB  
77 cultures after cell lysis are instead characterized by an excessively low hysteresis  
78 squareness <sup>23,24</sup>(Table 1, Fig. 1). Thus, current interpretations of these magnetic assemblages  
79 appear to miss structures possessing the high hysteresis squareness typical of SD particles,  
80 as well as a mixed FORC signature with a central ridge and VO contributions.

81 Possible candidates for such structures include multiple strands of magnetosomes  
82 produced by certain MTB <sup>25</sup>, and specific, mechanically meaningful forms of chain collapse,  
83 such as double strands resulting from bending single-stranded chains beyond the elastic  
84 limit <sup>26</sup>. Single- and multi-stranded chains in MTB are in a native SD state that maximizes

85 the total magnetic moment of the cell, with the magnetic moments of all magnetosomes  
86 being parallel to the chain axis <sup>27</sup>. This is the only possible magnetic configuration for  
87 single-stranded chains, but not for multiple strands, in which intermediate states with lower  
88 magnetic moments can be nucleated with the application of strong external fields <sup>27</sup>.  
89 Intermediate states are formed when the magnetic moment of one strand is reversed with  
90 respect to the others, or when the magnetic moments of individual particles form complex  
91 patterns <sup>28</sup>. The common characteristic of these so-called flux-closure (FC) configurations  
92 is the formation of closed field line loops inside the chain body, which suppress the external  
93 stray field of SD states. Transitions between SD and FC states, and vice-versa, generate  
94 FORC diagram contributions outside the region occupied by the central ridge, resembling  
95 those of VO <sup>15,16</sup> or strongly interacting SD particles <sup>29</sup>. Unlike these latter systems with a  
96 small hysteresis squareness, native multi-stranded chains are characterized by squareness  
97 values close to 0.5 due to the stability of SD states, including the native one, in zero or very  
98 small ambient fields <sup>30</sup>.

99 Here, we propose that the unresolved magnetic signature of magnetofossils can be  
100 explained by combinations of intact or elastically deformed single- or multi-stranded  
101 magnetosome chains (non-collapsed), and fold-collapsed chains. Nucleation and annihilation  
102 of FC magnetic states explains the VO signatures in FORC diagrams of magnetofossil-bearing  
103 sediments, while the strong uniaxial anisotropy of intact and collapsed  
104 chains ensures that they still possess SD-like remanence and SD-like hysteresis squareness  
105 of ~0.5. Our claim is supported by micromagnetic simulations of single- and double-  
106 stranded chains made of equant and prismatic magnetosomes. These simulations should be  
107 validated using MTB with multi-stranded chains. However, no such MTB are available for

108 cultures in the laboratory. To overcome this limitation, we produced a mutant of the  
109 magnetotactic bacterium *Magnetospirillum magneticum* strain AMB-1 (AMB-1)  
110 synthesizing folded magnetite chains, whose looped structure is topologically identical to  
111 double-stranded chain configurations in wild-type uncultured MTB. From magnetic  
112 measurements and off-axis electron holography characterizations, we demonstrate that the  
113 folded chains produced by the AMB-1 mutant generate FC magnetic signatures similar to  
114 those obtained with our micromagnetic simulations, while lacking the hysteresis  
115 squareness of the simulations and of natural magnetofossil signatures. This demonstrates  
116 that the unique magnetic fingerprints of magnetofossils originate from the magnetosome  
117 arrangements with strong uniaxial anisotropy, distinct from that of clusters and looped  
118 chains. This work resolves longstanding and ongoing controversies about the interpretation  
119 of sedimentary sources of SD magnetite, establishing a theoretical and experimental  
120 framework that explains the magnetofossil signature and provides insights into the  
121 diversity of ancient MTB populations.

122

## 123 **Results**

124 **Micromagnetic modeling.** To determine whether native multi-stranded and fold-  
125 collapsed magnetosome chains could explain the combination of SD and VO properties  
126 with SD hysteresis squareness typical of MTB, we first modeled their FORC distributions.  
127 Micromagnetic modeling of high-resolution FORC measurements was performed for  
128 selected magnetosome morphologies and chain configurations representative of intact or  
129 elastically deformed chains, and of fold-collapsed chains. The magnetic properties of the  
130 simulated structures are determined mainly by two factors: the anisotropy of individual

131 magnetosomes which is controlled by their shape and crystal orientation, and magnetostatic  
132 interactions. Magnetosome shapes can be classified as equant (cuboctahedral, octahedral),  
133 elongated (prismatic, elongated octahedral), and highly elongated (tooth- and bullet-  
134 shaped) <sup>25</sup>. These categories form well-defined clusters of crystal sizes within the SD  
135 stability range <sup>31,32</sup>(Fig. S1).

136 The geometry of intact single-stranded chains is controlled by the gap between magneto-  
137 somes, the decrease of immature magnetosomes sizes towards the chain ends (tapering),  
138 and elastic bending. Magnetosomes in multi-stranded chains are staggered: each  
139 magnetosome in one strand faces the gap between two magnetosomes of a nearby strand  
140 (Fig. S2). This arrangement favors the formation of strand bundles with a consistent  
141 magnetic polarity and minimizes repulsive forces <sup>27</sup>. Contrastingly, magnetosomes in fold-  
142 collapsed chains are arranged side-to-side, and size tapering occurs only at one end, the  
143 other end being the kink point of the native chain. The side-to-side magnetosome  
144 arrangement maximizes lateral attractive forces <sup>28</sup>.

145 The full variability of natural chains can be only partially reproduced, because most  
146 geometric parameters must be extrapolated from few observations. Therefore, we selected  
147 combinations of two magnetosome morphologies (cuboctahedral and prismatic), and three  
148 chain geometries (single-stranded, native double-stranded, and double-stranded from  
149 collapse by folding), as representative examples of magnetic endmembers dictated by the  
150 magnetosome aspect ratio (equant *vs.* elongated), and the existence of flux-closure  
151 configurations (single- *vs.* double-stranded). FORC measurements were simulated after  
152 generating ~40,000 synthetic chains with random orientations and realistic geometries for

153 each of the six categories obtained by combining the above-mentioned magnetosome  
154 morphologies and chain configurations (Figs. S3-S6, for double-stranded chain examples).

155 The simulated FORC diagrams of single-stranded chains (Fig. 2A and 2D) possess all  
156 the expected characteristics that have been predicted theoretically<sup>33</sup> and verified on cultured  
157 MTB<sup>24</sup>. The corresponding coercivity distributions are slightly narrower and biased  
158 towards ~30% higher fields with respect to the so-called biogenic soft (BS) and hard (BH)  
159 components commonly found in magnetofossil-rich sediments and attributed to intact  
160 chains of equidimensional and elongated magnetosomes, respectively<sup>19,24,35</sup>. Simulated  
161 FORC diagrams of double-stranded chain configurations feature flux-closure signatures  
162 (Fig. 2B and 2E). These features are fully developed only in fold-collapsed chains of equant  
163 magnetosomes, as seen by the constricted hysteresis loop (Fig. S7) and the clearly  
164 identifiable positive and negative doublets above and below the central ridge (Fig. 2C).

165 However, contrary to the AMB-1 mutant (see below) and to existing examples of magnetic  
166 systems featuring this type of FORC signature<sup>15,22,36</sup>, the hysteresis squareness is only slightly  
167 lowered with respect to the SD case ( $M_r/M_s = 0.471$ , with  $M_r$  and  $M_s$  corresponding to the  
168 remanent and saturation magnetizations, respectively) (Table 1, Fig. 1), and fully  
169 compatible with magnetofossil signatures<sup>20</sup>. Squareness values close to 0.5 for all simulated  
170 double-stranded chains means that they possess stable SD states in zero field, as observed  
171 on native chains<sup>37</sup>, and unlike the topologically equivalent structures of the AMB-1 mutant.

172 The SD stability of multi-stranded chains originates from their strong uniaxial anisotropy,  
173 which is not shared by other natural structures with FC states. Uniaxial anisotropy is further  
174 enhanced by magnetosome elongation and by the staggered crystal arrangement.

175 The central ridge coercivity distributions of double-stranded chains are remarkably  
176 similar to those of single-stranded chains made of the same type of magnetosomes, there-  
177 fore contributing in a similar manner to the so-called BS and BH coercivity components of  
178 magnetofossil signatures. The other coercivity distributions, on the other hand, contain  
179 additional low-field contributions related to FC nucleation and annihilation. In the case of  
180 equant magnetosomes, these contributions produce a second peak (fold-collapsed) or a  
181 shoulder (native) around 15 mT. In the case of prismatic magnetosomes, distributions are  
182 wider, and the peak position is lowered by ~10 mT with respect to the central ridge.

183 Our model thus reproduces well the unresolved magnetic signatures observed in  
184 sedimentary rocks. However, the unique association of this signature with single- and  
185 multi-stranded chains, which does not require previously proposed forms of chain collapse  
186 or alteration [e.g. clumping<sup>23</sup> and folding<sup>38</sup>], needs to be experimentally demonstrated.

187

188 **Mutant AMB-1 strain with looped chains.** Given that no MTB with multi-stranded  
189 chains are available in culture for laboratory experiments, we generated a mutant AMB-1  
190 strain making looped magnetosome chains (Fig. 3). Such mutant can serve as a useful term  
191 of comparison given by chain configuration with FC states. Magnetosome formation in  
192 MTB requires genes contained in a specific portion of the genome called the magnetosome  
193 island (MAI)<sup>39</sup>. AMB-1 genome also contains a small version of the magnetosome island  
194 called the magnetotaxis islet (MIS)<sup>40</sup>. The MIS contains several genes, some of which  
195 perform redundant functions with their homologs in the MAI<sup>41</sup>. Previous work in  
196 *Magnetospirillum gryphiswaldense* strain MSR-1 (MSR-1), a close relative of AMB-1,  
197 showed that the loss of the MAI gene *mamJ* results in collapse and aggregation of

198 magnetosome chains<sup>42</sup>. Surprisingly, the deletion of *mamJ* and its other MAI homolog *limJ*  
199 in AMB-1 does not produce collapsed chains and instead results in minor disruptions to  
200 the continuity of the chain<sup>43</sup>. We reasoned that redundant functions within the MIS might  
201 account for the dramatic differences between *mamJ* mutants in AMB-1 and MSR-1. Thus,  
202 a mutant strain ( $\Delta mamJ \Delta limJ \Delta MIS$ ) was produced by deleting the entire MIS and two MAI  
203 genes (*mamJ* and *limJ*) from AMB-1 genome. Unlike the *mamJ* MSR-1 mutant, which  
204 produces agglomerated magnetosomes, the phenotype of the AMB-1 mutant contains  
205 looped magnetosome chains with necklace structures located either at one of the poles or  
206 at the center of the cell (Fig. 3). Magnetite in the mutant strain falls in the stable SD size  
207 range<sup>31</sup>. The magnetic behavior of bacteria was assessed using the magnetic coefficient  
208 ( $C_{mag}$ ), which relies on the differential measurement of a culture's optical density when a  
209 magnet is oriented either vertically or horizontally close to the cell suspension.  $C_{mag}$  is  
210 defined as the ratio of the maximum and minimum optical density measured, and quantifies  
211 the capacity of bacteria to orientate along an external magnetic field.  $C_{mag}$  values at the end  
212 of bacterial growth were  $1.82 \pm 0.09$  and  $1.09 \pm 0.01$  for wild-type and mutant AMB-1,  
213 respectively, demonstrating a very limited orientation capability for the mutant strain.

214 **Native magnetic states of wild-type and mutant AMB-1 cells.** The low  $C_{mag}$  values in  
215 the mutant AMB-1 strain suggests that its looped magnetosome chain configurations  
216 possess a low net magnetic moment. We thus investigated the magnetic state of wild-type  
217 and mutant AMB-1 strains at the population level by comparing the magnetization of two  
218 different preparations of aqueous cell suspensions in a maximum external field of 2 mT,  
219 using a vibrating-sample magnetometer (VSM). The external field is sufficiently large to  
220 partially align the cells, but not large enough to alter their native magnetic configuration.

221 The first preparation contains cells directly taken from the culture: in this case, the  
222 suspension magnetization is expected to be proportional to the mean strength of the native  
223 magnetic moments. In the second preparation, the suspension has been previously exposed  
224 to a 200 mT field. This field is sufficiently strong to reset the native magnetic states,  
225 replacing them with a saturation remanent state carrying the maximum magnetic moment  
226 that can be maintained in a null field.

227 Wild-type cells containing straight magnetite chains already possess a saturation rema-  
228 nent state. Exposing them to a large field will thus not change the magnetization of the  
229 suspension. In practice, a ~40% increase is observed after applying a 200 mT field (Fig.  
230 4A). This increase might be explained by the growth of aligned chain fragments with  
231 opposite native polarities within the same cell <sup>44</sup>. In this case, the application of a strong  
232 external field imparts the same polarity to all fragments, increasing the cell's total magnetic  
233 moment. A drastically different behavior is observed with the AMB-1 mutant: an 18-fold  
234 magnetization increase is obtained after applying a 200 mT field (Fig. 4D). Along with the  
235 magnetic behavior assays ( $C_{\text{mag}}$ ), this result indicates a vanishingly small native magnetic  
236 moment of the AMB-1 mutant, which is compatible with a FC configuration of its looped  
237 chains. The sigmoidal shape of the magnetization curve of the 200 mT-treated suspension  
238 in fields up to 2 mT can be explained by the concurring effects of cell alignment, which is  
239 responsible for the curve slope above 0.5 mT, and the additional magnetization induced by  
240 the reversible rotation of the magnetic moments of individual crystals towards the external  
241 field. The induced magnetization is larger for high-energy magnetic configurations, such  
242 as those created in the AMB-1 mutant by the application of a strong field, than for low-

243 energy magnetic configurations, such as the native SD state of wild-type cells and the  
244 native FC state of the mutant.

245 **Electron holography.** VSM characterizations of mutant AMB-1 demonstrated a  
246 vanishingly small magnetic moment of the bacteria which may be related to the looped  
247 chain structure. To further confirm this hypothesis, we mapped the magnetic flux in the  
248 fold-collapsed magnetosome chains at the single-crystal level with off-axis electron  
249 holography. Electron holography is an interferometric method that can correlate  
250 morphological and local magnetic characterizations of magnetic materials. It allows  
251 quantitative mapping of the in-plane flux inside the magnetite chains produced by AMB-1  
252 at the nanometer scale. Mapping of the magnetic flux in magnetosome chains produced in  
253 wild-type AMB-1 (Figs. 4B and 4C) indicates that the magnetic moments of individual  
254 magnetosomes are nearly parallel to the chain axis, as previously observed<sup>45</sup>. In contrast,  
255 necklace structures of the mutant strain display a closed magnetic flux (Figs. 4E and 4F).  
256 This configuration has a zero-net magnetic moment, up to small fluctuations due to  
257 asymmetries (*e.g.* larger crystals on one side of the structure), confirming the origin of the  
258 vanishing native magnetic moments of the AMB-1 mutant deduced from magnetic  
259 measurements.

260 **FORC measurements.** The analysis of the mutant AMB-1 shows that its looped chains  
261 can be a reasonable mimic for naturally occurring multi-stranded chains as well as fold-  
262 collapsed magnetosome chains. Thus, it was selected to test the hypothesis that multi-  
263 stranded chain configurations can generate FORC signatures similar to the unresolved ones  
264 observed in sediments. The magnetic properties of the wild-type and mutant AMB-1 strains  
265 were characterized with high-resolution FORC analyses using a VSM. Wild-type AMB-1

266 (Fig. 5A) shows the central ridge typical of isolated uniaxial SD particles and magnetosome  
267 chains, as well as a negative-positive doublet in the lower quadrant, nearly antisymmetric  
268 about the  $B_c = -B_a$  diagonal, produced by the reversible rotation of magnetic moments in  
269 the applied field <sup>17</sup>. The magnetically viscous contribution of immature chains is  
270 recognizable from the presence of a vertical ridge along  $B_c = 0$  <sup>16</sup>, and from the central ridge  
271 extending down to  $B_c = 0$ . These chains are made of magnetosomes with sizes close to the  
272 lower SD stability limit (between 12 and 17 nm for equant crystals) (Fig. 3) <sup>32</sup>. The  
273 hysteresis squareness ( $M_r/M_s = 0.475$ ) is slightly smaller than the ideal value for single-  
274 stranded chains, probably because of a small superparamagnetic contribution associated  
275 with isolated immature crystals as confirmed by electron microscopy (Fig. 3). The  
276 coercivity distributions obtained from FORC data subsets possess similar, unimodal  
277 characteristics with a peak at 28-30 mT and the right tail extending to a maximum of 60-  
278 70 mT.

279 The mutant AMB-1 strain shares these features (*i.e.* central ridge, viscous component  
280 and rotations of magnetic moments in the applied field), albeit over different field ranges,  
281 but also exhibits additional contributions (Fig. 5B), consisting of a doublet of positive lobes  
282 at  $B_c \approx 12$  mT and  $B_a \approx \pm 8$  mT, and a doublet of negative lobes at  $B_c \approx 25$  mT and  $B_a \approx \pm 3$   
283 mT, almost symmetrically arranged above and below the central ridge. These lobes are the  
284 typical hallmark of FC nucleation and annihilation <sup>15</sup>, as seen with VO particles <sup>22</sup> and small  
285 magnetosome clusters produced by the  $\Delta mamJ$  mutant of MSR-1 <sup>36</sup>. The hysteresis loop is  
286 slightly constricted (Fig. S8) with a much smaller squareness (Table1, Fig. 1), which is  
287 caused by necklace-like magnetosome arrangements that do not possess stable SD-like  
288 magnetic states in a null field due to insufficient or absent uniaxial anisotropy. Constricted

289 hysteresis loops are typically the result of bimodal coercivity distributions, which, in this  
290 case, consist of a main peak at  $\sim 2$  mT, and a shoulder at  $\sim 25$  mT (Fig. 5D). The main peak  
291 of the central ridge, close to the origin, is caused by thermally activated transitions between  
292 SD states of structures made of immature magnetosomes, including isolated crystals. FC  
293 nucleation from the negative SD state (feature 4 in Fig. 5B) contributes additionally to the  
294 main peak of the other two coercivity distributions, explaining its larger amplitude with  
295 respect to the central ridge. A single mechanism, namely the annihilation of FC states  
296 around  $+25$  mT, explains the existence of a shoulder with similar amplitude in all three  
297 coercivity distributions.

298 The lack of low-coercivity central ridge contributions from FC nucleation is a common  
299 feature of all magnetic systems with coexisting SD-like and FC states and is a key point  
300 for understanding magnetofossil signatures. Another key point is the lowered hysteresis  
301 squareness of the AMB-1 mutant. Its incompatibility with the magnetic signature of  
302 magnetofossil-rich sediments permits the exclusion of looped magnetosome  
303 configurations, such as those produced by laboratory-induced chain collapse<sup>47</sup> and by the  
304 self-avoiding random walk algorithm used to simulate magnetofossil chains with various  
305 collapse degrees<sup>38,48</sup>.

306 In summary, the combination of magnetic modelling and measurements demonstrate  
307 that magnetic assemblages with coexisting central ridge, SD-like and VO (features 4, 5 and  
308 6 in Fig. 5B) states can be explained by the presence of multi-stranded magnetosome chains  
309 rather than multiple components with distinct origins and magnetic states. The  
310 conservation of high hysteresis squareness typical of intact magnetosome chains points to

311 native multi-stranded chains produced by specific MTB lineages, while lower hysteresis  
312 squareness being incompatible with aligned magnetosome particles also indicates the  
313 presence of fold-collapsed chains.

## 314 **Discussion**

315 Magnetic assemblages showing concurrent fingerprints of central ridges (no  
316 magnetostatic interactions) and vertical scattering of the FORC distribution (large  
317 magnetostatic interactions) were previously interpreted as mixings of several magnetite  
318 sources including magnetofossils, magnetosome clusters, MD and VO particles<sup>19,49</sup>. These  
319 sources have various origins and provide insights into the geobiological history of the  
320 sediments hosting the magnetic assemblages. However, mixings of the above-mentioned  
321 magnetic sources cannot provide a satisfying explanation for the high hysteresis squareness  
322 typical of intact magnetosome chains<sup>20</sup>. Our work demonstrates that the magnetic  
323 signatures of these sediments can be explained by the sole presence of MTB producing  
324 multi-stranded magnetosome chains.

325 From micromagnetic simulations and FORC measurements, we demonstrated that the  
326 main characteristics of unresolved magnetofossil signatures can be reproduced by  
327 endmember structures consisting of native single- and double-stranded magnetosome  
328 chains, as well as fold-collapsed chains. All simulated structures contribute to the FORC  
329 central ridge and produce hysteresis loops with squareness values comprised between  
330 ~0.47 and 0.5. Double-stranded and fold-collapsed chains bear FORC signatures associated  
331 with the nucleation and annihilation of FC states where the two strands carry opposite  
332 magnetizations. A comparison of double-stranded chain simulations with the topologically

333 identical necklace structures produced by the AMB-1 mutant strain shows that the elevated  
334 hysteresis squareness of magnetofossils is due to the stabilization of SD magnetic states by  
335 the strong uniaxial anisotropy of linear chain structures. This anisotropy is responsible for  
336 the unique combination of SD and FC characteristics of magnetofossil signatures among  
337 known natural sources of magnetite particles. Destruction of the native chain anisotropy,  
338 as in magnetosome clusters obtained from laboratory extraction or produced by  $\Delta mamJ$   
339 mutants of the MSR-1 magnetotactic strain<sup>36</sup>, changes the original magnetic signature in a  
340 manner that is incompatible with the hysteresis properties of magnetofossil-rich sediment  
341 (Fig. 1), mainly because of an excessive squareness lowering. Complete chain collapse is  
342 therefore not expected to occur in sediment. Looped chains, as produced by the AMB-1  
343 mutant and by the algorithm used for micromagnetic simulations in ref.<sup>48</sup>, possess  
344 intermediate properties between those of native chains and SD particle clusters, which can  
345 be explained by the low-dimensionality of such structures. Closed chain loops, such as  
346 those produced by the AMB-1 mutant strain, are incompatible with sedimentary signatures  
347 (Fig. 1). On the other hand, widely open chain loops with hysteresis squareness values  
348 compatible with those of SD particles in sediment [Fig. 5a in ref.<sup>38</sup>] resemble bended single-  
349 stranded chains used in our simulation. The very subdued FORC contributions above the  
350 central ridge generated by these single-stranded chains configurations, however, do not  
351 reflect the FORC signature associated with SD-sized magnetite particles in magnetofossil-  
352 rich sediments (feature 2 in Fig. 6A). This natural signature, together with hysteresis  
353 squareness values close to 0.5, cannot be obtained from single-stranded chains alone,  
354 regardless of how much their native geometry is disrupted by the algorithm used in ref.<sup>48</sup>,

355 and therefore requires significant contributions from native multi-stranded chains or fold-  
356 collapsed chains that preserve the native uniaxial anisotropy.

357 Modeling and experiments on the AMB-1 mutant agree, but it is critical to see whether  
358 the observed patterns also appear in magnetofossil-rich sediments. A direct comparison  
359 between the FORC signatures of simulated chains and of *in situ* <1  $\mu\text{m}$  particles in a  
360 magnetofossil-rich sediment <sup>29</sup> reveals additional important insights. For this purpose, a  
361 composite FORC diagram has been generated using a mixture of the six chain structures  
362 simulated in this work (Fig. 6B). The chosen composition is arbitrary, since the natural  
363 proportions of equant and prismatic magnetosomes, and possibly also of single- and multi-  
364 stranded chains, is controlled by environmental factors <sup>7-9</sup>. The resulting FORC diagram  
365 shares striking similarities with the natural sediment example, but also important  
366 differences. Both diagrams feature a central ridge, but the coercivity range of simulations  
367 is comprised between ~20 and ~130 mT, while the natural central ridge contains significant  
368 contributions also in the 0-20 mT range. The existence of a minimum magnetofossil  
369 coercivity threshold in the simulations is explainable by the uniaxial anisotropy of non-  
370 looped chain structures. Immature magnetosomes at the chain ends, which have been  
371 included in the simulations, do not change this scenario, since they are strongly coupled to  
372 the rest of the chain. Thermal relaxation, which has not been considered in the simulations,  
373 tend to reduce the effective coercivity by an amount known as fluctuation field, thus  
374 shifting the central ridge toward lower fields <sup>46</sup>. A large coercivity reduction with respect to  
375 the simulation results can be excluded because (i) only a very minor fraction of observed  
376 magnetofossil sizes fall close to the lower SD stability limit (Fig. S2), as confirmed also  
377 by hysteresis squareness values close to 0.5, and (ii) the vertical offset of the central ridge,

378 which is comparable with the amplitude of the fluctuation field <sup>50</sup>, is  $\leq 0.5$  mT in  
379 magnetofossil-bearing sediment ( $\sim 0.4$  mT in Fig. 6A).

380 The interpretation of the low-coercivity range ( $< 20$  mT) of the central ridge is uncertain.  
381 Short chain fragments of 1-3 equant magnetosomes possess significantly lower coercivities  
382 than fully developed chains <sup>38</sup>, and can therefore contribute to the central ridge over this  
383 range. It is not known whether such fragments are produced by MTB under natural, slow-  
384 growing conditions, or if longer chains are naturally fragmented through adhesion of  
385 segments of the same chain to different sediment particles. Well-dispersed, nearly equidi-  
386 mensional SD particles, produced for instance by dissimilatory iron reduction in sediment  
387 <sup>51</sup> or during soil formation <sup>52</sup> can also contribute to the central ridge in the 0-20 mT range.  
388 The existence of low-coercivity contributions in the central ridge of most sediments means  
389 that biogenic and inorganic origins of SD magnetite particles, as postulated for the  
390 Paleocene-Eocene Thermal Maximum, are not mutually exclusive <sup>53,54</sup>.

391 Other FORC signatures of our micromagnetic simulations are qualitatively similar to  
392 those of magnetofossil-bearing sediments, including the slight asymmetry between the  
393 upper and the lower quadrant, and the abrupt  $B_c$ -termination of FC contributions (feature 2  
394 in Fig. S6). The contour lines of the simulated FORC are clearly affected by localized  
395 contributions of FC nucleation and annihilation of individual chain endmembers, which  
396 are not completely merged into a smooth distribution as in the natural counterpart. Small  
397 negative amplitudes above the central ridge are also not completely cancelled. This is  
398 understandable considering that simulations were limited to few, well-defined geometries.  
399 For instance, single- and multi-stranded chains made of bullet- or tooth-shaped magneto-  
400 somes were not included. Multi-stranded chains of bullet-shaped magnetosomes are

401 characterized by similarly elevated hysteresis squareness values as our double-stranded  
402 simulations, with a central ridge peaking at  $\sim 60$  mT<sup>55</sup>. This intermediate coercivity range  
403 would fill the gaps between simulated chains of equidimensional and prismatic  
404 magnetosomes, making the resulting FORC diagram more similar to that of natural  
405 magnetofossils.

406 Magnetic fingerprints have become an essential tool for magnetofossil identification (SI  
407 appendix). The different FORC signatures of intact chains on the one hand, and fold-  
408 collapsed or multi-stranded chains on the other, make the exact magnetic fingerprint of  
409 magnetofossils depend, to a certain extent, on the original MTB composition and degree  
410 of single-stranded chain preservation, yielding variable proportions of the BS and BH  
411 coercivity components<sup>34</sup>, and of central ridge and FC contributions to the FORC diagram  
412 (Table 1). This means that PCA analyses of magnetofossil-rich sedimentary sequences  
413 deposited under changing environmental conditions likely require more than one  
414 endmember to capture the variability of magnetofossil fingerprints. For instance, changes  
415 in the proportion of single- and double-stranded chains yield different relative contributions  
416 of the central ridge and FC features in the FORC diagrams, resulting in at least two  
417 endmembers: one dominated by the signature elements of single-stranded chains (central  
418 ridge and negative contributions in the lower quadrant, near the  $B_c$  axis), and the other  
419 dominated by those of multi-stranded chains (FC nucleation and annihilation contributions  
420 in the upper and lower quadrant). Variable proportions of single and multi-stranded chains  
421 can split the magnetofossil signature into two PCA endmembers that do not necessarily  
422 correspond to the physical signature of the two groups: for instance, the central ridge of  
423 both types of chains can go into one endmember, and the lobes of two-state chains into

424 another endmember, possibly together with the VO signatures of lithogenic inputs <sup>56</sup>, if  
425 these co-vary with the magnetofossil content as in certain pelagic environments <sup>8</sup>. This  
426 might explain why some endmembers interpreted as magnetofossils contain the signatures  
427 of two-state chains [e.g. EM2 in Figs. 8 and 10 of ref. <sup>49</sup>], while other do not [e.g. EM2 in  
428 Fig. 11 of ref. <sup>57</sup>].

429 Magnetic measurements have been used to obtain the *in situ* sedimentary FORC  
430 signature of SD magnetite <sup>50</sup>, including non-central ridge contributions that are specific to  
431 multi-stranded chains. Such measurements are of paleontological interest and could  
432 provide a temporal resolution on the evolution of magnetosome formation in MTB <sup>4</sup>. Only  
433 bacteria belonging to the more ancestral Delta-proteobacteria and Nitrospirae phyla were  
434 thought to produce multi-stranded chains of magnetosomes <sup>58</sup>. However, they have been  
435 now identified in the more recent Alpha-proteobacteria and Gamma-proteobacteria phyla  
436 <sup>59,60</sup>. Therefore, multi-stranded chain configuration has no specific phylogenetic distribution  
437 and might instead correspond to an adaptation to specific environments. In MTB,  
438 magnetosomes are aligned along cytoskeletal filaments made of actin-like proteins <sup>61</sup>.  
439 Among them, the protein MamK is ubiquitously conserved in all known MTB. Bacteria  
440 forming multiple magnetosome chains contain several copies of genes encoding actin-like  
441 proteins in addition to MamK <sup>62</sup>. We can thus hypothesize that genetic factors are  
442 responsible for multi-stranded chain configurations <sup>62</sup>. They may include gene duplication  
443 events <sup>39</sup>, or horizontal gene transfers (*i.e.* an exchange of genetic material through direct  
444 physical interactions between two organisms) <sup>63</sup>. Once the genetic basis of chain  
445 configurations is fully understood, the methodology we describe in this work can be used

446 to provide a temporal constrain on evolutionary events that occurred in one of the oldest  
447 and more diverse group of biomineralizing organisms.

## 448 **Material and methods**

449 **Deletion plasmid construction and generation of the  $\Delta mamJ\Delta limJ\Delta MIS$  AMB-1**  
450 **mutant strain.** Detailed procedures for plasmid construction and AMB-1 transformation  
451 are provided in SI appendix.

452 **Bacterial cultures.** *Magnetospirillum magneticum* strain AMB-1 (ATCC700264) and  
453 mutant AMB-1 strain were cultivated following ATCC recommendations in 500-mL  
454 screw-caped bottles until end of the exponential phase. Bottles were filled with 300 mL of  
455 growth medium, and placed in a glove box with controlled atmosphere (10% O<sub>2</sub>, 90% N<sub>2</sub>)  
456 at 30°C after inoculation (1/100). The sole iron source in bacterial growth medium was  
457 Fe(III)-citrate added at 150  $\mu$ M.

458 **Transmission electron microscopy.** Cells were deposited on copper grids coated with  
459 a Formvar and carbon films, and characterized with a FEI Tecnai 12 transmission electron  
460 microscope operating at 120 kV. Magnetite length and width were measured using the  
461 ImageJ software.

462 **Native magnetic moment measurements.** AMB-1 cultures were centrifuged (8 000  
463 rpm, 10 min) and suspended in 10 mL of phosphate buffer (PBS). 100  $\mu$ L of cell suspension  
464 were transferred in plastic vials (diameter of 4 mm), and placed in a Lakeshore Micro-Mag  
465 3900 VSM for acquisition of remanent magnetizations at room temperature.

466       **Off-axis electron holography.** Both wild-type and mutant AMB-1 strains were  
467 cultivated in 10-mL glass tubes following the protocol described above. Cells were  
468 centrifuged (8 000 rpm, 10 min) and suspended in 100  $\mu$ L of phosphate buffer (PBS). They  
469 were then deposited on copper grids coated with an ultra-thin carbon membrane. Off-axis  
470 electron holography was carried out using a Hitachi HF3300C microscope operated at 300  
471 kV and equipped with a cold field emission gun and a spherical aberration corrector (CEOS  
472 B-Corr). Electron holography experiments were performed in a specific corrected Lorentz  
473 mode, allowing a spatial resolution down to 0.5 nm in a magnetic field-free sample  
474 environment <sup>64</sup>. All holograms were recorded in a 2-biprism configuration to avoid artifacts  
475 linked to Fresnel fringes and to set separately the interference area size and the fringe  
476 spacing <sup>65</sup>. The fringe spacing is equal to 1 nm (7 pixels) allowing for a spatial resolution  
477 of 1.5 nm for the treated magnetic phase images. The exposure time was set to 1 nm using  
478 dynamic automation acquisition for removing instabilities and applying the fringe  $\pi$ -shift  
479 method <sup>66,67</sup>. Phase and amplitude images were extracted from the holograms by using  
480 homemade software based on fast-Fourier transform approach. The magnetic and  
481 electrostatic contributions have been separated by acquiring two holograms for which the  
482 sample has been switched upside down (flipped 180°): the magnetic contribution was  
483 obtained by evaluating the difference of the phase images from the two holograms divided  
484 by two.

485       **Micromagnetic modeling.** Micromagnetic modeling has been performed in two steps.  
486 First, randomly oriented synthetic chains for each of the six configurations have been  
487 generated. Magnetosome-specific control parameters include size, shape, and crystal axes  
488 orientation according to realistic distributions obtained from the literature. Chain-specific

489 control parameters include magnetosome gaps, number of crystals, size tapering, and chain  
490 bending within the elastic limit. The configuration of double-stranded chains is additionally  
491 controlled by the lag of one strand with respect to the other, and by twisting about a  
492 common axis. The distributions of these parameters have been empirically chosen to match  
493 examples reported in the literature. Next, micromagnetic calculations have been performed  
494 to simulate FORC measurements with a resolution of 1 mT. These calculations are based  
495 on the minimization of the total magnetic energy resulting from magnetocrystalline and  
496 shape anisotropy of individual crystals, the Zeeman energy in the applied field, and the  
497 energy of magnetostatic interactions between pairs of crystals. Simulated FORC  
498 measurements have been further processed with VARIFORC<sup>68</sup>, using minimal smoothing  
499 parameters to eliminate the statistical noise caused by the relatively limited number of  
500 simulated chains. Further details are given in the SI Appendix.

501

502 **FORC measurements.** AMB-1 cultures were recovered by centrifugation (8 000 rpm,  
503 10 min). Bacterial pellets were transferred in a 1.5-mL eppendorf tube and dried at room  
504 temperature under anoxic conditions in a glove box ( $[O_2] < 1\text{ ppm}$ ) to prevent magnetite  
505 oxidation. Samples were stored under anoxic conditions until before being measured with  
506 a Lakeshore 8600 VSM.

507

508 **ACKNOWLEDGMENTS.** AK and MA are supported by grants through the National  
509 Science Foundation (1504681) and National Institutes of Health (R35GM127114). MA is  
510 supported by grant through the *Fondation pour la Recherche Médicale*  
511 (ARF201909009123). The research leading to these results has received funding from the

512 European Union Horizon 2020 research and innovation program under grant agreement  
513 No. 823717 – ESTEEM3. The authors acknowledge the French National Research Agency  
514 under the “Investissement d’Avenir” program reference No. ANR-10-EQPX-38-01 and the  
515 “Conseil Régional Midi-Pyrénées” and the European FEDER for financial support within  
516 the CPER program. This work was also supported by the international associated  
517 laboratory M<sup>2</sup>OZART.  
518

## 519 References

- 520 1. Egli, R., Fabio, F. & Roberts, A. Introduction to ‘Magnetic ironminerals in sediments and their  
521 relation to geologic processes, climate, and the geomagnetic field’. *Global and Planetary*  
522 *Change* **110**, 259–263 (2013).
- 523 2. Fortin, D. & Langley, S. Formation and occurrence of biogenic iron-rich minerals. *Earth-Sci.*  
524 *Rev.* **72**, 1–19 (2005).
- 525 3. Uebe, R. & Schueler, D. Magnetosome biogenesis in magnetotactic bacteria. *Nat. Rev.*  
526 *Microbiol.* **14**, 621–637 (2016).
- 527 4. Lin, W. *et al.* Origin of microbial biomineralization and magnetotaxis during the Archean.  
528 *Proc. Natl. Acad. Sci. U. S. A.* **114**, 2171–2176 (2017).
- 529 5. Simmons, S. L., Sievert, S. M., Frankel, R. B., Bazylinski, D. A. & Edwards, K. J.  
530 Spatiotemporal distribution of marine magnetotactic bacteria in a seasonally stratified coastal  
531 salt pond. *Appl. Environ. Microbiol.* **70**, 6230–6239 (2004).
- 532 6. Flies, C. B. *et al.* Diversity and vertical distribution of magnetotactic bacteria along chemical  
533 gradients in freshwater microcosms. *FEMS Microbiol. Ecol.* **52**, 185–195 (2005).
- 534 7. Hesse, P. P. Evidence for bacterial palaeoecological origin of mineral magnetic cycles in oxic  
535 and sub-oxic Tasman Sea sediments. *Mar. Geol.* **117**, 1–17 (1994).
- 536 8. Roberts, A. P. *et al.* Magnetotactic bacterial abundance in pelagic marine environments is  
537 limited by organic carbon flux and availability of dissolved iron. *Earth Planet. Sci. Lett.* **310**,  
538 441–452 (2011).
- 539 9. Usui, Y., Yamazaki, T. & Saitoh, M. Changing Abundance of Magnetofossil Morphologies in  
540 Pelagic Red Clay Around Minamitorishima, Western North Pacific. *Geochemistry,*  
541 *Geophysics, Geosystems* **18**, 4558–4572 (2017).
- 542 10. McCausland, H. C. & Komeili, A. Magnetic genes: Studying the genetics of biomineralization  
543 in magnetotactic bacteria. *PLOS Genetics* **16**, e1008499 (2020).
- 544 11. Petersen, N., von Dobeneck, T. & Vali, H. Fossil bacterial magnetite in deep-sea sediments  
545 from the South Atlantic Ocean. *Nature* **320**, 611–615 (1986).

- 546 12. Kopp, R. E. & Kirschvink, J. L. The identification and biogeochemical interpretation of fossil  
547 magnetotactic bacteria. *Earth-Sci. Rev.* **86**, 42–61 (2008).
- 548 13. Larrasoana, J. C. *et al.* Paleomagnetic and paleoenvironmental implications of magnetofossil  
549 occurrences in late Miocene marine sediments from the Guadalquivir Basin, SW Spain. *Front.*  
550 *Microbiol.* **5**, 71 (2014).
- 551 14. Ouyang, T. *et al.* Variable remanence acquisition efficiency in sediments containing biogenic  
552 and detrital magnetites: Implications for relative paleointensity signal recording. *Geochem.*  
553 *Geophys. Geosyst.* **15**, 2780–2796 (2014).
- 554 15. Roberts, A. P. *et al.* Resolving the Origin of Pseudo-Single Domain Magnetic Behavior.  
555 *Journal of Geophysical Research: Solid Earth* **122**, 9534–9558 (2017).
- 556 16. Lascu, I., Einsle, J. F., Ball, M. R. & Harrison, R. J. The Vortex State in Geologic Materials:  
557 A Micromagnetic Perspective. *Journal of Geophysical Research: Solid Earth* **123**, 7285–7304  
558 (2018).
- 559 17. Egli, R., Chen, A. P., Winklhofer, M., Kodama, K. P. & Horng, C.-S. Detection of  
560 noninteracting single domain particles using first-order reversal curve diagrams. *Geochem.*  
561 *Geophys. Geosyst.* **11**, Q01Z11 (2010).
- 562 18. Roberts, A. P., Chang, L., Heslop, D., Florindo, F. & Larrasoana, J. C. Searching for single  
563 domain magnetite in the “pseudo-single-domain” sedimentary haystack: Implications of  
564 biogenic magnetite preservation for sediment magnetism and relative paleointensity  
565 determinations. *J. Geophys. Res.-Solid Earth* **117**, (2012).
- 566 19. Heslop, D., Roberts, A. P. & Chang, L. Characterizing magnetofossils from first-order reversal  
567 curve (FORC) central ridge signatures. *Geochemistry, Geophysics, Geosystems* **15**, 2170–2179  
568 (2014).
- 569 20. Ludwig, P. *et al.* Characterization of primary and secondary magnetite in marine sediment by  
570 combining chemical and magnetic unmixing techniques. *Global and Planetary Change* **110**,  
571 321–339 (2013).

- 572 21. Muxworthy, A., Williams, W. & Virdee, D. Effect of magnetostatic interactions on the  
573 hysteresis parameters of single-domain and pseudo-single-domain grains. *J. Geophys. Res.-*  
574 *Solid Earth* **108**, (2003).
- 575 22. Dumas, R. K., Li, C.-P., Roshchin, I. V., Schuller, I. K. & Liu, K. Magnetic fingerprints of  
576 sub-100 nm Fe dots. *Phys. Rev. B* **75**, 134405 (2007).
- 577 23. Kobayashi, A. *et al.* Experimental observation of magnetosome chain collapse in  
578 magnetotactic bacteria: Sedimentological, paleomagnetic, and evolutionary implications.  
579 *Earth Planet. Sci. Lett.* **245**, 538–550 (2006).
- 580 24. Li, J., Wu, W., Liu, Q. & Pan, Y. Magnetic anisotropy, magnetostatic interactions and  
581 identification of magnetofossils. *Geochem. Geophys. Geosyst.* **13**, Q10Z51 (2012).
- 582 25. Amor, M., Mathon, F. P., Monteil, C. L., Busigny, V. & Lefevre, C. T. Iron-biomineralizing  
583 organelle in magnetotactic bacteria: function, synthesis and preservation in ancient rock  
584 samples. *Environ. Microbiol.* **22**, 3611–3632 (2020).
- 585 26. Shcherbakov, V. P., Winklhofer, M., Hanzlik, M. & Petersen, N. Elastic stability of chains of  
586 magnetosomes in magnetotactic bacteria. *Eur. Biophys. J. Biophys.* **4**, 319–326 (1997).
- 587 27. Hanzlik, M., Winklhofer, M. & Petersen, N. Pulsed-field-remnance measurements on  
588 individual magnetotactic bacteria. *J. Magn. Magn. Mater.* **248**, 258–267 (2002).
- 589 28. Varón, M. *et al.* Dipolar Magnetism in Ordered and Disordered Low-Dimensional  
590 Nanoparticle Assemblies. *Sci Rep* **3**, 1234 (2013).
- 591 29. Carvallo, C., Dunlop, D. J. & Özdemir, Ö. Experimental comparison of FORC and remanent  
592 Preisach diagrams. *Geophys. J. Int.* **162**, 747–754 (2005).
- 593 30. Pan, Y. X. *et al.* Rock magnetic properties of uncultured magnetotactic bacteria. *Earth Planet.*  
594 *Sci. Lett.* **237**, 311–325 (2005).
- 595 31. Muxworthy, A. R. & Williams, W. Critical single-domain/multidomain grain sizes in  
596 noninteracting and interacting elongated magnetite particles: Implications for magnetosomes.  
597 *J. Geophys. Res.-Solid Earth* **111**, (2006).

- 598 32. Newell, A. J. Transition to superparamagnetism in chains of magnetosome crystals.  
599 *Geochemistry, Geophysics, Geosystems* **10**, (2009).
- 600 33. Newell, A. J. A high-precision model of first-order reversal curve (FORC) functions for single-  
601 domain ferromagnets with uniaxial anisotropy. *Geochemistry, Geophysics, Geosystems* **6**,  
602 (2005).
- 603 34. Egli, R. Characterization of Individual Rock Magnetic Components by Analysis of Remanence  
604 Curves, 1. Unmixing Natural Sediments. *Studia Geophys. Geod.* **48**, 391–446 (2004).
- 605 35. Chen, A. P. *et al.* Magnetic properties of uncultivated magnetotactic bacteria and their  
606 contribution to a stratified estuary iron cycle. *Nat. Commun.* **5**, 4797 (2014).
- 607 36. Katzmann, E. *et al.* Analysis of Magnetosome Chains in Magnetotactic Bacteria by Magnetic  
608 Measurements and Automated Image Analysis of Electron Micrographs. *Appl. Environ.*  
609 *Microbiol.* **79**, 7755–7762 (2013).
- 610 37. Li, J. *et al.* Crystal growth of bullet-shaped magnetite in magnetotactic bacteria of the  
611 Nitrospirae phylum. *J. R. Soc. Interface* **12**, 20141288 (2015).
- 612 38. Chang, L., Harrison, R. J. & Berndt, T. A. Micromagnetic simulation of magnetofossils with  
613 realistic size and shape distributions: Linking magnetic proxies with nanoscale observations  
614 and implications for magnetofossil identification. *Earth Planet. Sci. Lett.* **527**, 115790 (2019).
- 615 39. Murat, D., Quinlan, A., Vali, H. & Komeili, A. Comprehensive genetic dissection of the  
616 magnetosome gene island reveals the step-wise assembly of a prokaryotic organelle. *Proc.*  
617 *Natl. Acad. Sci. U. S. A.* **107**, 5593–5598 (2010).
- 618 40. Rioux, J.-B. *et al.* A Second Actin-Like MamK Protein in *Magnetospirillum magneticum*  
619 AMB-1 Encoded Outside the Genomic Magnetosome Island. *PLOS ONE* **5**, e9151 (2010).
- 620 41. Abreu, N. *et al.* Interplay between Two Bacterial Actin Homologs, MamK and MamK-Like,  
621 Is Required for the Alignment of Magnetosome Organelles in *Magnetospirillum magneticum*  
622 AMB-1. *J. Bacteriol.* **196**, 3111–3121 (2014).
- 623 42. Scheffel, A. *et al.* An acidic protein aligns magnetosomes along a filamentous structure in  
624 magnetotactic bacteria. *Nature* **440**, 110–114 (2006).

- 625 43. Draper, O. *et al.* MamK, a bacterial actin, forms dynamic filaments in vivo that are regulated  
626 by the acidic proteins MamJ and LimJ. *Mol. Microbiol.* **82**, 342–354 (2011).
- 627 44. Le Nagard, L. *et al.* Magnetite magnetosome biomineralization in *Magnetospirillum*  
628 *magneticum* strain AMB-1: A time course study. *Chem. Geol.* **530**, 119348 (2019).
- 629 45. Dunin-Borkowski, R. E. *et al.* Magnetic microstructure of magnetotactic bacteria by electron  
630 holography. *Science* **282**, 1868–1870 (1998).
- 631 46. Lanci, L. & Kent, D. V. Forward Modeling of Thermally Activated Single-Domain Magnetic  
632 Particles Applied to First-Order Reversal Curves. *Journal of Geophysical Research: Solid*  
633 *Earth* **123**, 3287–3300 (2018).
- 634 47. Philipse, A. P. & Maas, D. Magnetic colloids from magnetotactic bacteria: Chain formation  
635 and colloidal stability. *Langmuir* **18**, 9977–9984 (2002).
- 636 48. Harrison, R. J. & Lascu, I. FORCulator: A micromagnetic tool for simulating first-order  
637 reversal curve diagrams. *Geochemistry, Geophysics, Geosystems* **15**, 4671–4691 (2014).
- 638 49. Lascu, I. *et al.* Magnetic unmixing of first-order reversal curve diagrams using principal  
639 component analysis. *Geochemistry, Geophysics, Geosystems* **16**, 2900–2915 (2015).
- 640 50. Berndt, T. A., Chang, L., Wang, S. & Badejo, S. Time-Asymmetric FORC Diagrams: A New  
641 Protocol for Visualizing Thermal Fluctuations and Distinguishing Magnetic Mineral Mixtures.  
642 *Geochemistry, Geophysics, Geosystems* **19**, 3056–3070 (2018).
- 643 51. Moskowitz, B., Frankel, R. & Bazylinski, D. Rock Magnetic Criteria for the Detection of  
644 Biogenic Magnetite. *Earth Planet. Sci. Lett.* **120**, 283–300 (1993).
- 645 52. Geiss, C. E., Egli, R. & Zanner, C. W. Direct estimates of pedogenic magnetite as a tool to  
646 reconstruct past climates from buried soils. *J. Geophys. Res.-Solid Earth* **113**, (2008).
- 647 53. Kent, D. V. *et al.* A case for a comet impact trigger for the Paleocene/Eocene thermal maximum  
648 and carbon isotope excursion. *Earth Planet. Sci. Lett.* **211**, 13–26 (2003).
- 649 54. Lippert, P. C. & Zachos, J. C. A biogenic origin for anomalous fine-grained magnetic material  
650 at the Paleocene-Eocene boundary at Wilson Lake, New Jersey. *Paleoceanography* **22**,  
651 PA4104 (2007).

- 652 55. Li, J. *et al.* Biomineralization, crystallography and magnetic properties of bullet-shaped  
653 magnetite magnetosomes in giant rod magnetotactic bacteria. *Earth and Planetary Science*  
654 *Letters* **293**, 368–376 (2010).
- 655 56. Chang, L. *et al.* Widespread occurrence of silicate-hosted magnetic mineral inclusions in  
656 marine sediments and their contribution to paleomagnetic recording. *Journal of Geophysical*  
657 *Research: Solid Earth* **121**, 8415–8431 (2016).
- 658 57. Channell, J. E. T. *et al.* Magnetic record of deglaciation using FORC-PCA, sortable-silt grain  
659 size, and magnetic excursion at 26 ka, from the Rockall Trough (NE Atlantic). *Geochemistry,*  
660 *Geophysics, Geosystems* **17**, 1823–1841 (2016).
- 661 58. Deng, A. *et al.* In vitro assembly of the bacterial actin protein MamK from ' Candidatus  
662 Magnetobacterium casensis' in the phylum Nitrospirae. *Protein Cell* **7**, 267–280 (2016).
- 663 59. Taoka, A., Kondo, J., Oestreicher, Z. & Fukumori, Y. Characterization of uncultured giant rod-  
664 shaped magnetotactic Gammaproteobacteria from a freshwater pond in Kanazawa, Japan.  
665 *Microbiology*, **160**, 2226–2234 (2014).
- 666 60. Zhang, H. *et al.* Magnetotactic Coccus Strain SHHC-1 Affiliated to Alphaproteobacteria Forms  
667 Octahedral Magnetite Magnetosomes. *Front. Microbiol.* **8**, (2017).
- 668 61. Müller, F. D., Schüler, D. & Pfeiffer, D. A Compass To Boost Navigation: Cell Biology of  
669 Bacterial Magnetotaxis. *Journal of Bacteriology* **202**, (2020).
- 670 62. Kolinko, S., Richter, M., Gloeckner, F.-O., Brachmann, A. & Schueler, D. Single-cell  
671 genomics of uncultivated deep-branching magnetotactic bacteria reveals a conserved set of  
672 magnetosome genes. *Environ. Microbiol.* **18**, 21–37 (2016).
- 673 63. Monteil, C. L. *et al.* Repeated horizontal gene transfers triggered parallel evolution of  
674 magnetotaxis in two evolutionary divergent lineages of magnetotactic bacteria. *ISME J.* **14**,  
675 1783–1794 (2020).
- 676 64. Snoeck, E. *et al.* Off-Axial Aberration Correction using a B-COR for Lorentz and HREM  
677 Modes. *Microscop. Microanal.* **20**, 932–933 (2014).

- 678 65. Harada, K., Tonomura, A., Togawa, Y., Akashi, T. & Matsuda, T. Double-biprism electron  
679 interferometry. *Appl. Phys. Lett.* **84**, 3229–3231 (2004).
- 680 66. Gatel, C., Dupuy, J., Houdellier, F. & Hýtch, M. J. Unlimited acquisition time in electron  
681 holography by automated feedback control of transmission electron microscope. *Appl. Phys.*  
682 *Lett.* **113**, 133102 (2018).
- 683 67. Volkov, V. V., Han, M. G. & Zhu, Y. Double-resolution electron holography with simple  
684 Fourier transform of fringe-shifted holograms. *Ultramicroscopy* **134**, 175–184 (2013).
- 685 68. Egli, R. VARIFORC: An optimized protocol for calculating non-regular first-order reversal  
686 curve (FORC) diagrams. *Global and Planetary Change* **110**, 302–320 (2013).  
687

688 **Tables**

689 **Table 1.** Summary of measured and modelled magnetic properties of MTB and magneto-  
 690 fossils.  $\chi_{\text{ARM}}/\text{IRM}$  is the so-called ARM ratio, and  $M_r/M_s$  is the ratio between the magneti-  
 691 zation associated by the central ridge and the saturation remanent magnetization (see SI  
 692 Appendix S2).

<b>Structure</b>	<b>Reference</b>	$M_r/M_s$	$\chi_{\text{ARM}}/\text{IRM}$ (mm/A)	$M_r/M_s$
Sediment (<1 $\mu\text{m}$ )	<sup>20</sup>	0.47	2–3	0.65
<i>Single-stranded</i>				
Cultured MTB	<sup>24,51</sup>	0.50	3.1–3.7	0.65
AMB-1	This study, <sup>24</sup>	0.48–0.50	1.38	0.79
Simulated	This study	0.49–0.50	—	0.71–0.72
Simulated (random walk)	<sup>38</sup>	0.32–0.38	—	?
<i>Multi-stranded</i>				
MTB (multi-stranded)	<sup>30</sup>	0.47–0.51	0.5–0.8	?
Simulated (2 strands native)	This study	0.47–0.49	—	0.40–0.42
Simulated (fold-collapsed)	This study	0.47–0.50	—	0.37–0.38
<i>Clumps and loops</i>				
Extracted magnetosomes	<sup>24</sup>	0.22	0.23	?
<i>M. gyphiswaldense</i> $\Delta\text{mamJ}$	<sup>36</sup>	0.23	—	?
AMB-1 mutant	This study	0.31	—	0.53

693

694

695 **Figure captions**

696 **Fig. 1.**  $B_c/B_c$  vs.  $M_r/M_s$  diagram showing the hysteresis properties of intact cultured cells  
697 <sup>24,30,51</sup>, SD particles in a magnetofossil-rich sediment <sup>20</sup>, the AMB-1 mutant producing looped  
698 magnetosome arrangements (this work), and a  $\Delta mamJ$  mutant producing magnetosome 699  
clusters <sup>36</sup>. The properties of extracted magnetosomes <sup>24</sup>, micromagnetically simulated 700  
chains with increasing degree of looping <sup>38</sup>, and our micromagnetic simulations of intact 701  
and fold-collapsed chains are shown for comparison. Departures from  $M_r/M_s = 0.5$  for ideal, 702  
non-interacting, uniaxial SD particles (cultured cells), form trends with increasing slopes, 703  
from intact and fold-collapsed configurations with strong uniaxial anisotropy (intact & 704  
folded) to complete randomization (extracted magnetosomes), through the intermediate 705  
trend of looped chains (looped).

706

707 **Fig. 2.** Micromagnetic simulations of single-stranded, double-stranded, and fold-collapsed  
708 chains of equant and prismatic magnetosomes, respectively. For each configuration, the  
709 FORC diagram (top) and the corresponding coercivity distributions (bottom, thick lines)  
710 are shown. FORC diagrams share the same color scale with contours at  $\pm 2$ ,  $\pm 5$ , 10, 20, 60,  
711 60, and 80% of the maximum amplitude. The inset in each FORC diagram shows a  
712 representative simulated chain example. Coercivity distributions represented by thick lines  
713 correspond, from smallest to largest amplitude, to the central ridge ( $f_{cr}$ , red), the irreversible  
714 hysteresis ( $f_{irr}$ , green), and the DC demagnetization curve ( $f_{dcd}$ , dashed), respectively.  
715 Coercivity distributions represented by thin grey lines correspond to examples of BS (A-  
716 C) and BS (D-F) coercivity components obtained from AF demagnetization curves of  
717 ARM, after ref. <sup>34</sup>.

718 **Fig. 3.** Electron microscopy images of wild-type and mutant AMB-1 cells.

719

720 **Fig. 4.** Native magnetic states of wild-type AMB-1 and the AMB-1 mutant. Magnetization

721 of a suspension of (A) wild-type and (D) mutant AMB-1 cells in small fields varying

722 between  $\pm 2$  mT, before (black) and after (gray) saturation in a 200 mT field. Electron

723 microscopy and corresponding magnetic phase contours determined by off-axis electron

724 holography images of (B-C) wild-type and (E-F) mutant magnetite chains.

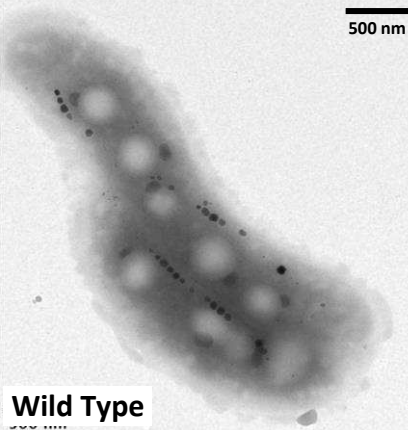
725

726 **Fig. 5.** Magnetic properties of wild-type AMB-1 and the AMB-1 mutant. (A-B) FORC  
 727 diagrams normalized by the saturation magnetization, with same logarithmically spaced  
 728 contours. Insets are schematic representations of the magnetization of an individual cell as  
 729 a function of the applied field. Numbers highlight the following features: 1 – central ridge  
 730 created by the magnetization jump through which the lowest curve merges with curve I; 2  
 731 – positive and negative contributions from reversible magnetic moment rotation (difference  
 732 between the slopes of consecutive curves); 3 — signatures of magnetically viscous  
 733 particles (vertical ridge and central ridge extending to the origin); 4 — nucleation of a  
 734 negative FC state from a negative SD state (contribution of the first magnetization jump in  
 735 curve III to the difference between curves II and III); 5 — annihilation of a positive FC  
 736 state (contribution of the magnetization jump in curve II to the difference between curves  
 737 I and II); 6 — same as 5, but for the difference between curve II and III; 7 — annihilation  
 738 of a negative FC state (contribution of the second magnetization jump in curve III to the  
 739 difference between curves II and III). (C-D) Coercivity distributions of wild-type AMB-1  
 740 and the AMB-1 mutant, obtained from subsets of FORC data:  $f_{ir}$  — irreversible component  
 741 of the ascending hysteresis branch,  $f_{sd}$  — DC demagnetization of  $M_{rs}$ ,  $f_{cr}$  — central ridge.  
 742 The shaded area represents the  $f_{ir}$  contribution of SD magnetic states that cannot exist in a  
 743 null field.

744 **Fig. 6.** Comparison between the FORC signature of SD particles in a magnetofossil-rich  
745 sediment and synthetic results. **(a)** FORC diagram of in-situ  $<1\mu\text{m}$  magnetite particles  
746 (mostly SD) in a pelagic sediment [data from ref. <sup>20</sup>]. **(b)** FORC diagram of a synthetic  
747 composite obtained from the six micromagnetically modelled chain structures, with the  
748 following relative contributions to the saturation magnetization, chosen for a visual match  
749 with (a): 21% (single-stranded chains of equant magnetosomes), 4% (single-stranded  
750 chains of prismatic magnetosomes), 42% (native double-stranded chains of equant  
751 magnetosomes), 8% (native double-stranded chains of prismatic magnetosomes), 21%  
752 (fold-collapsed chains of equant magnetosomes), 4% (fold-collapsed chains of prismatic  
753 magnetosomes). The same field range and contour levels with respect to the maximum  
754 amplitude are used in both plots to ease the comparison. Numbers highlight the following  
755 features: 1 — nucleation/annihilation of FC states, 2 — high-field limit of FC state  
756 nucleation/annihilation (asymmetric about the central ridge), 3 — residual negative  
757 amplitude from the annihilation of positive FC states, uncompensated by positive ampli-  
758 tudes from intermediate coercivity contributions.

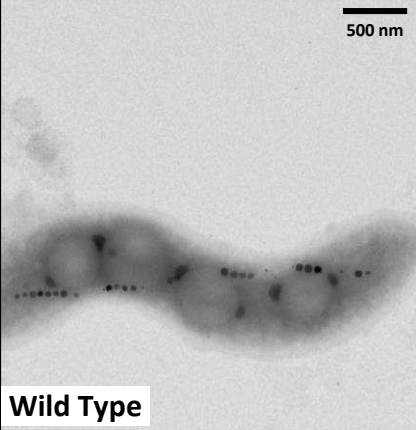
759

500 nm



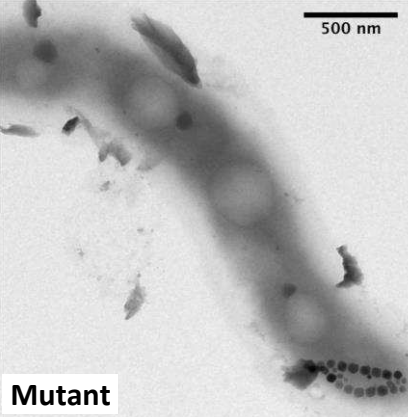
Wild Type

500 nm



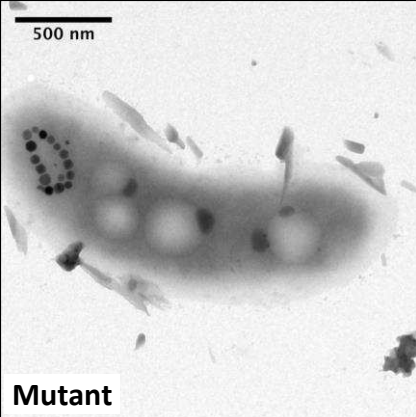
Wild Type

500 nm



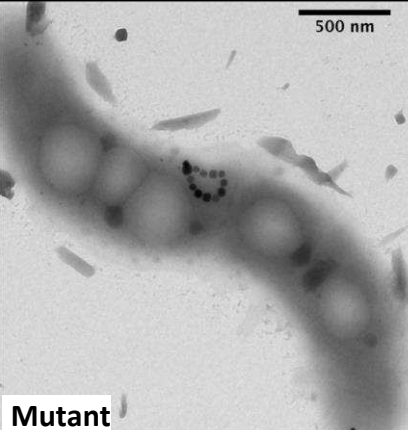
Mutant

500 nm



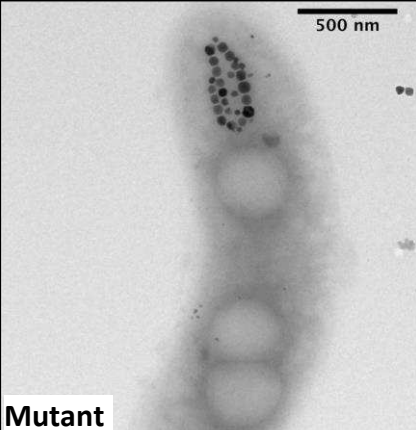
Mutant

500 nm

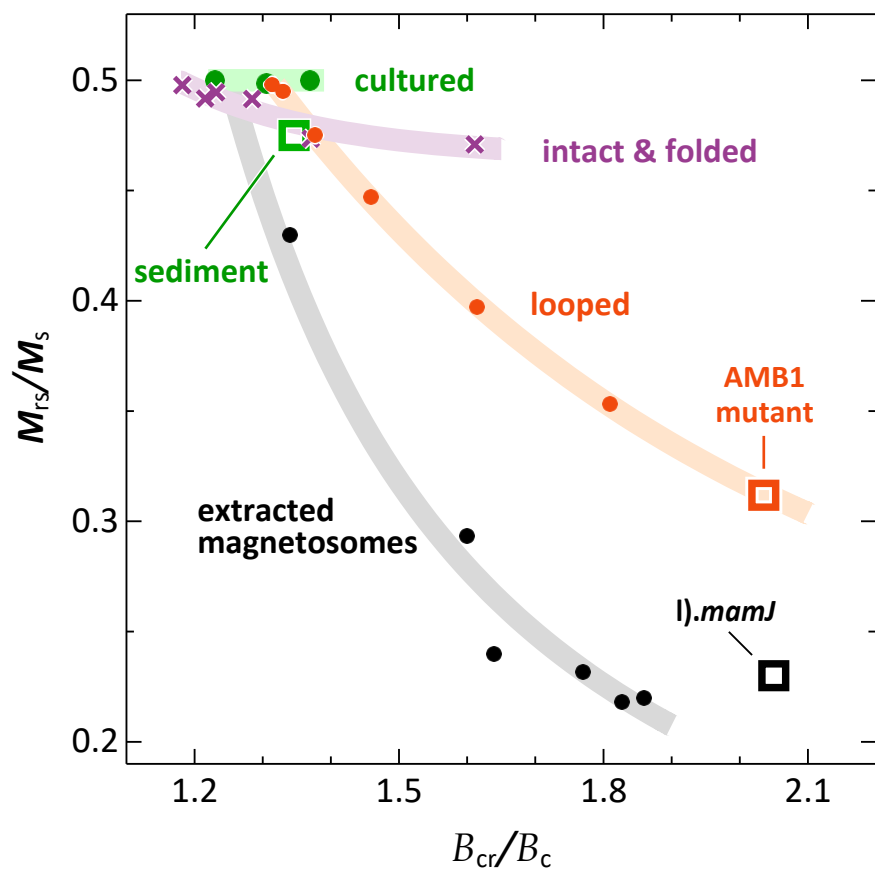


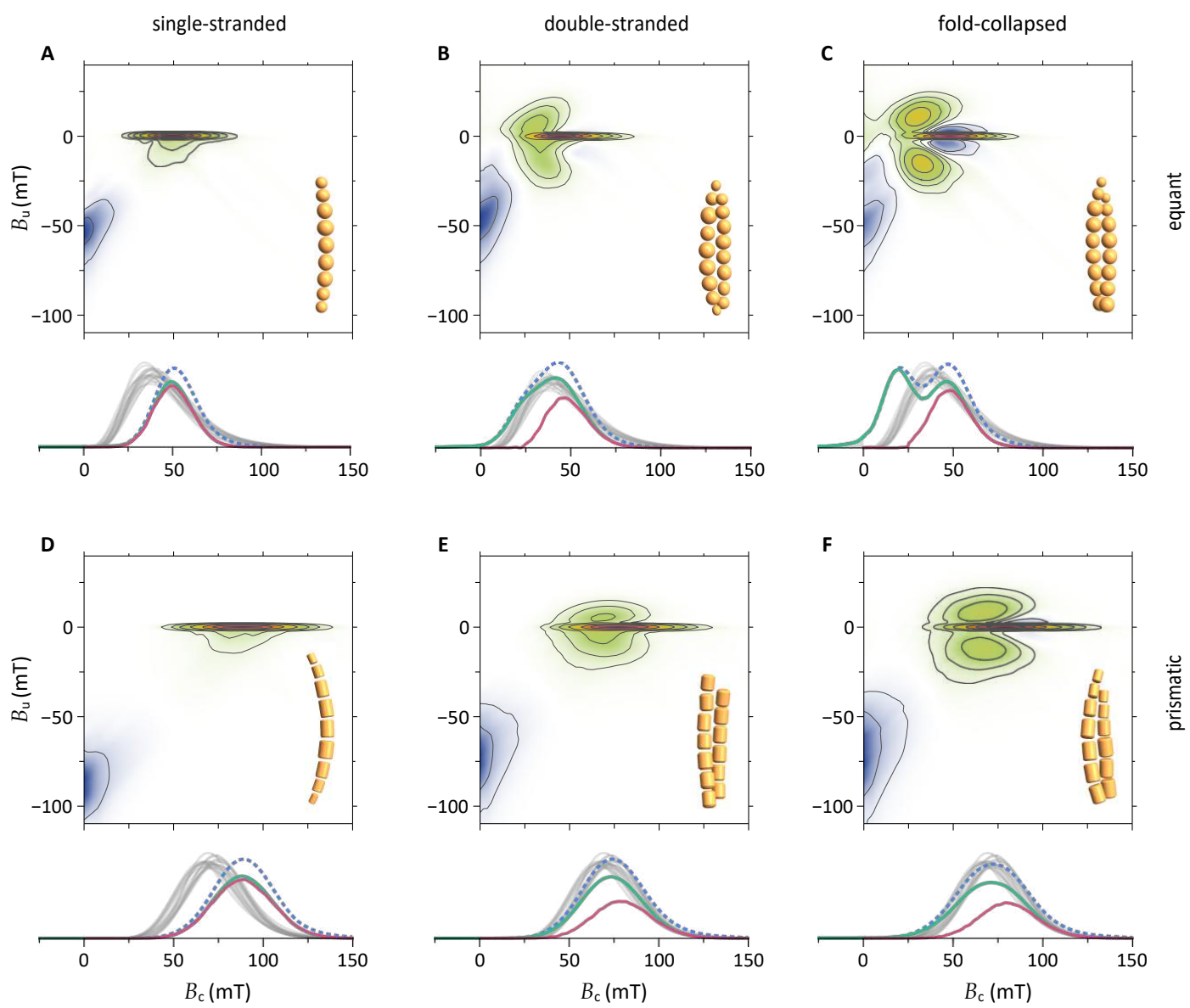
Mutant

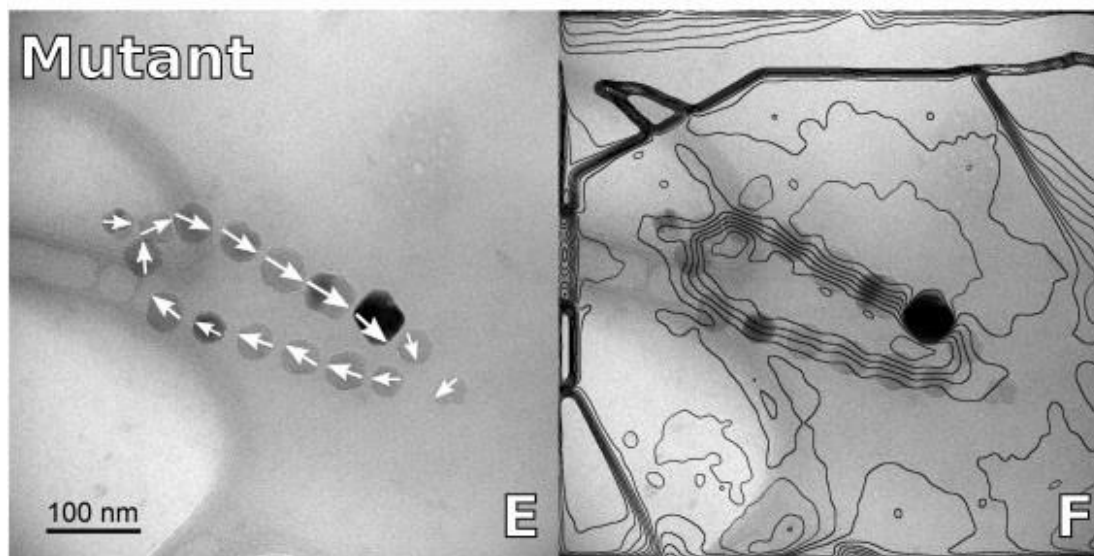
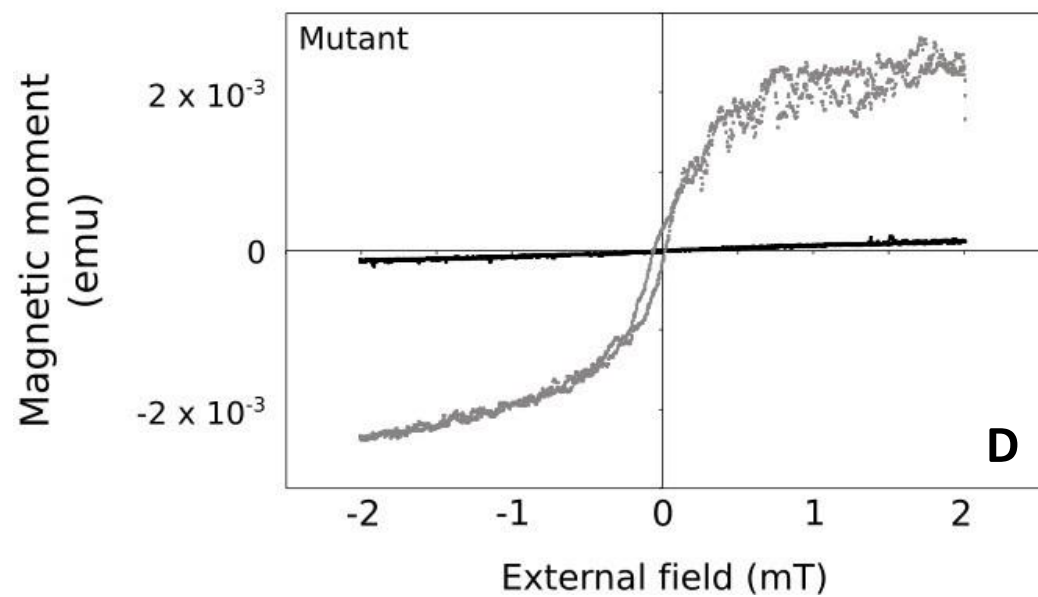
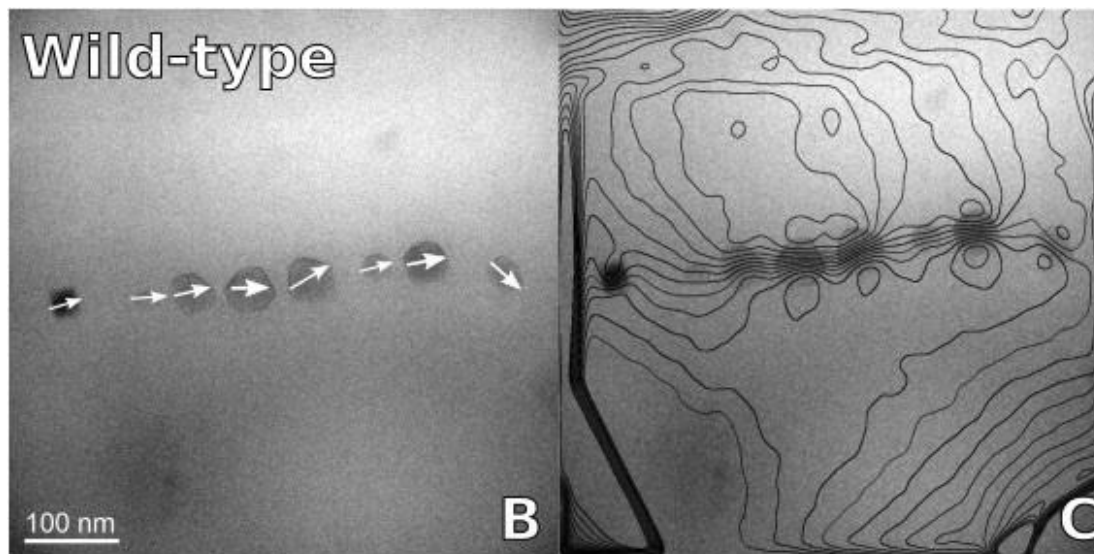
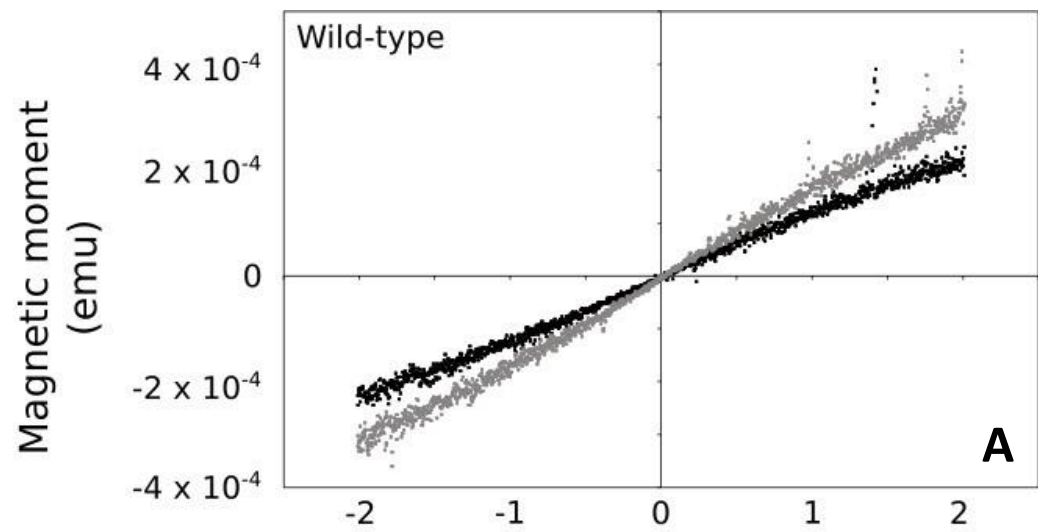
500 nm

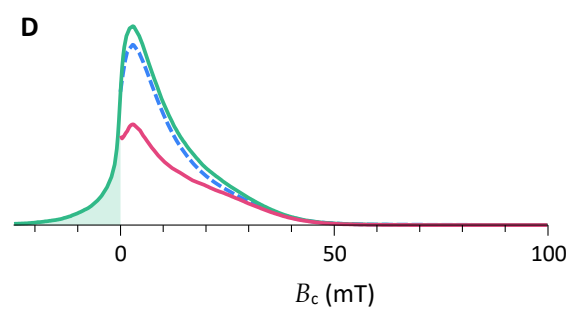
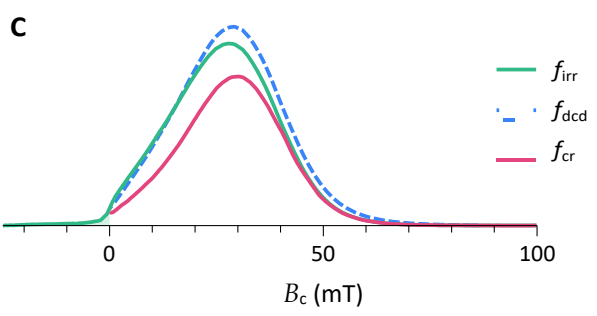
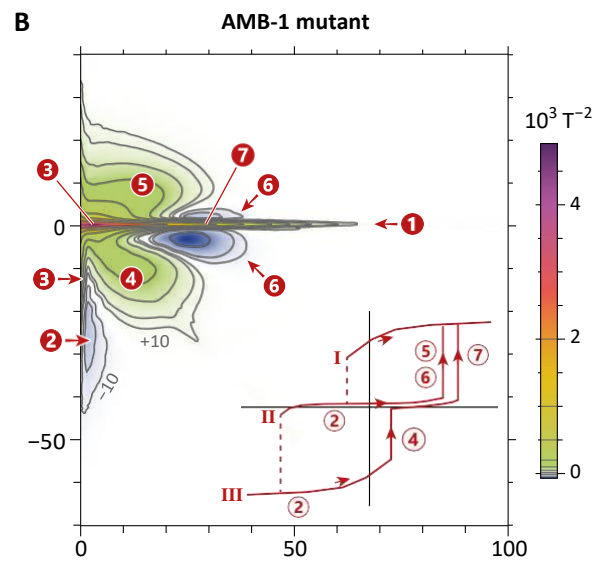
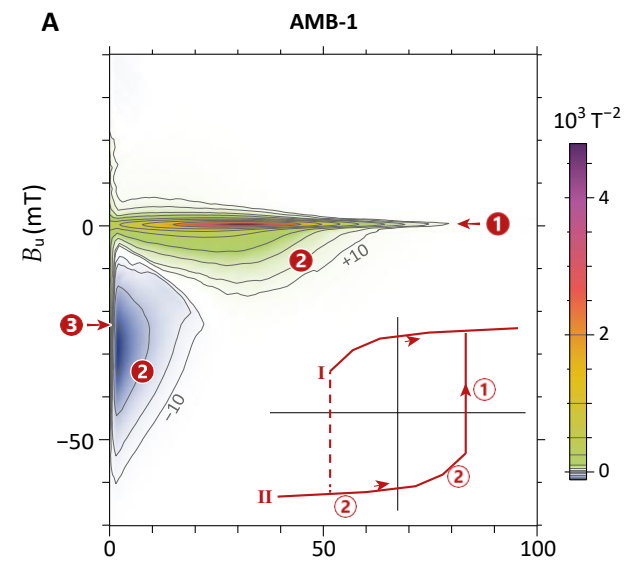


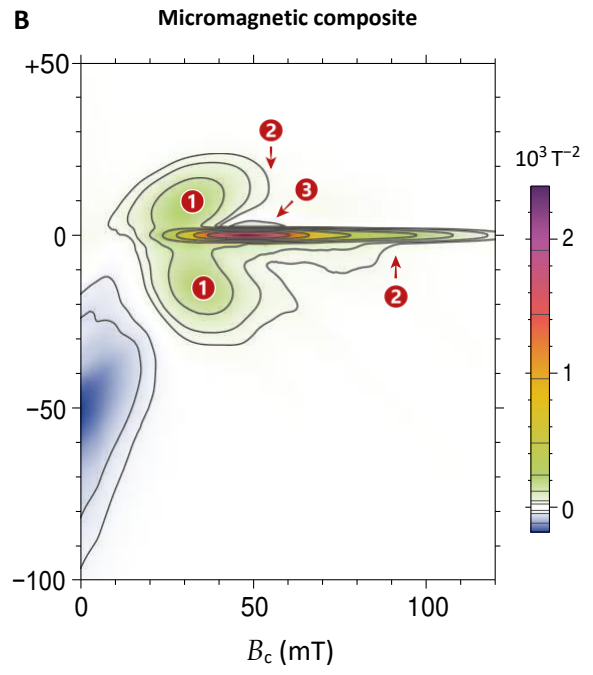
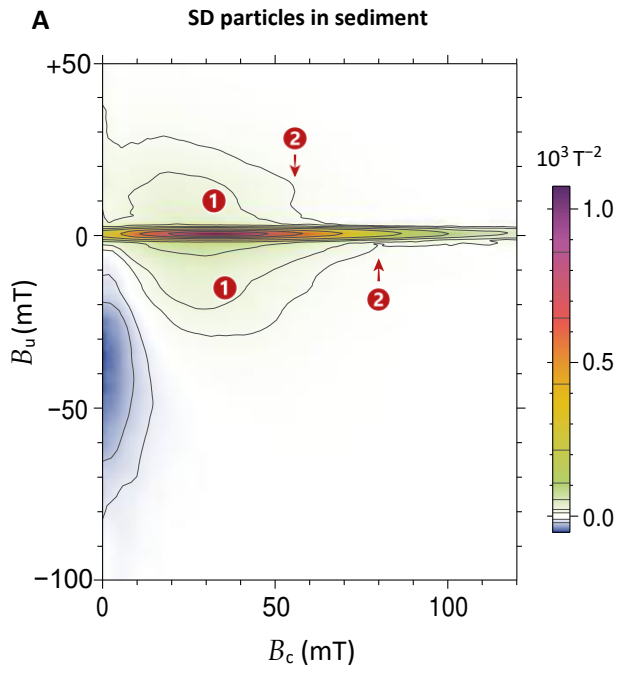
Mutant











# Figures

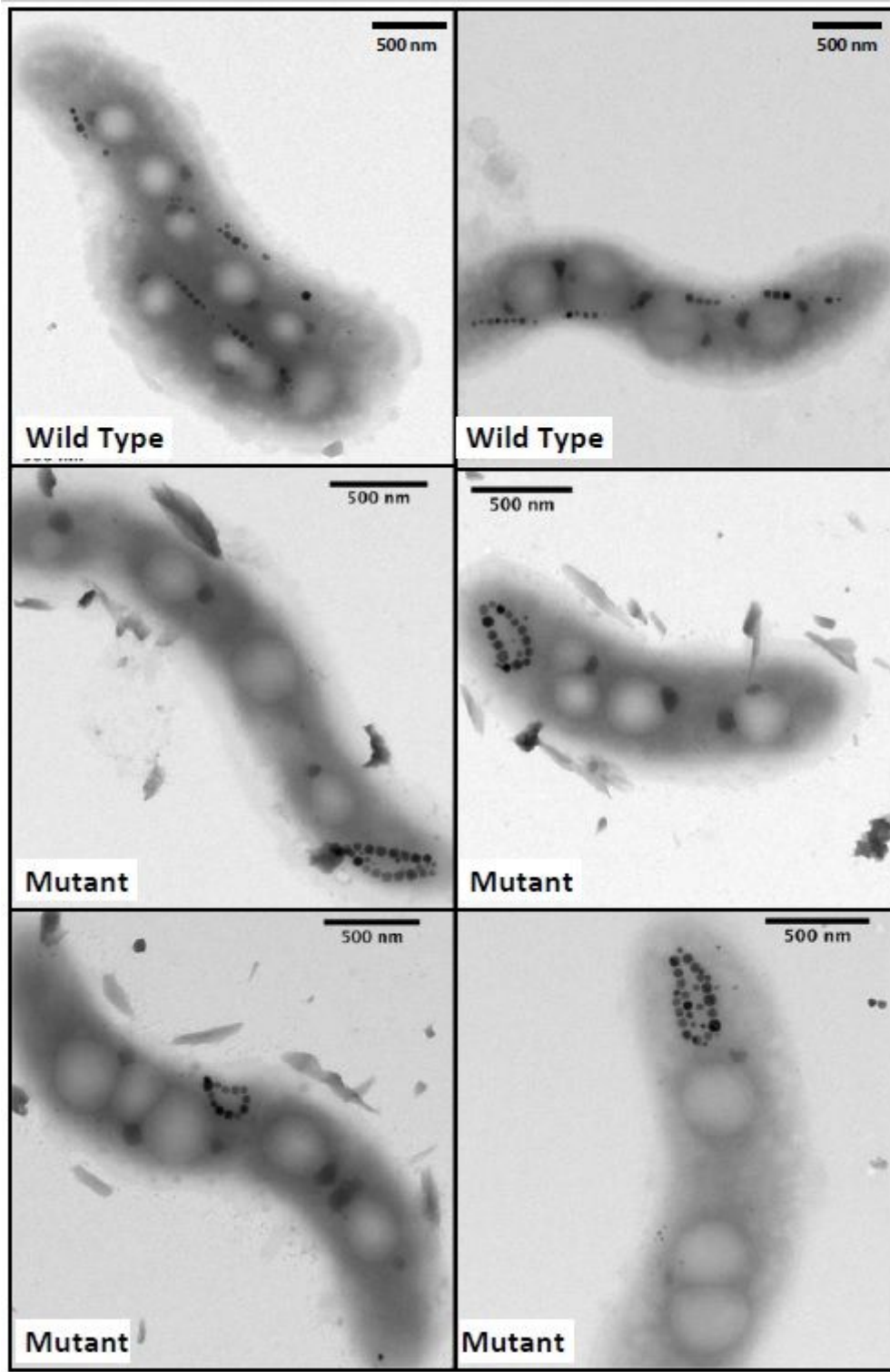
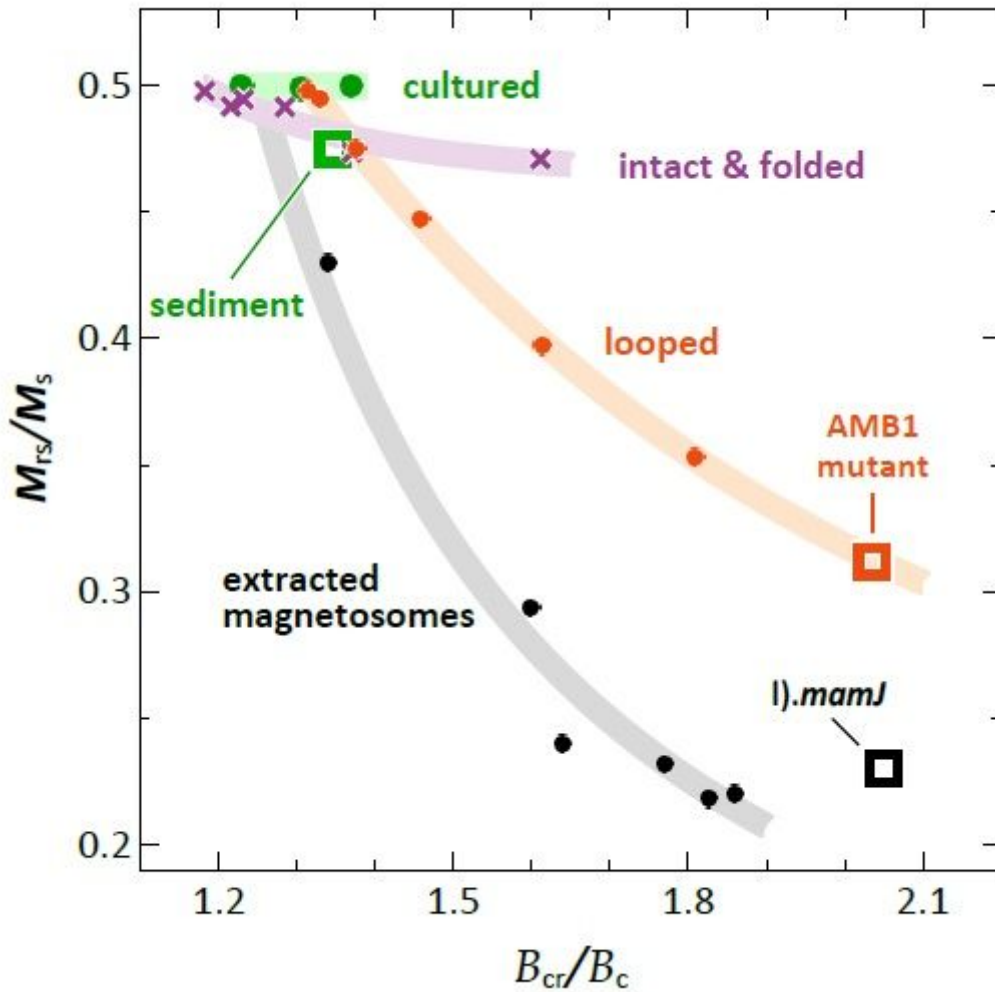


Figure 1

Bcr/Bc vs. Mrs/Ms diagram showing the hysteresis properties of intact cultured cells 24,30,51, SD particles in a magnetofossil-rich sediment 20, the AMB-1 mutant producing looped magnetosome arrangements (this work), and a  $\Delta$ mamJ mutant producing magnetosome clusters 36. The properties of

extracted magnetosomes 24, micromagnetically simulated chains with increasing degree of looping 38, and our micromagnetic simulations of intact and fold-collapsed chains are shown for comparison. Departures from  $M_{rs}/M_s = 0.5$  for ideal, non-interacting, uniaxial SD particles (cultured cells), form trends with increasing slopes, from intact and fold-collapsed configurations with strong uniaxial anisotropy (intact & folded) to complete randomization (extracted magnetosomes), through the intermediate trend of looped chains (looped).



**Figure 2**

Micromagnetic simulations of single-stranded, double-stranded, and fold-collapsed chains of equant and prismatic magnetosomes, respectively. For each configuration, the FORC diagram (top) and the corresponding coercivity distributions (bottom, thick lines) are shown. FORC diagrams share the same color scale with contours at  $\pm 2$ ,  $\pm 5$ , 10, 20, 60, 60, and 80% of the maximum amplitude. The inset in each FORC diagram shows a representative simulated chain example. Coercivity distributions represented by thick lines correspond, from smallest to largest amplitude, to the central ridge (fcr, red), the irreversible hysteresis (firr, green), and the DC demagnetization curve (fdcd, dashed), respectively. Coercivity distributions represented by thin grey lines correspond to examples of BS (A-C) and BS (D-F) coercivity components obtained from AF demagnetization curves of ARM, after ref. 34.

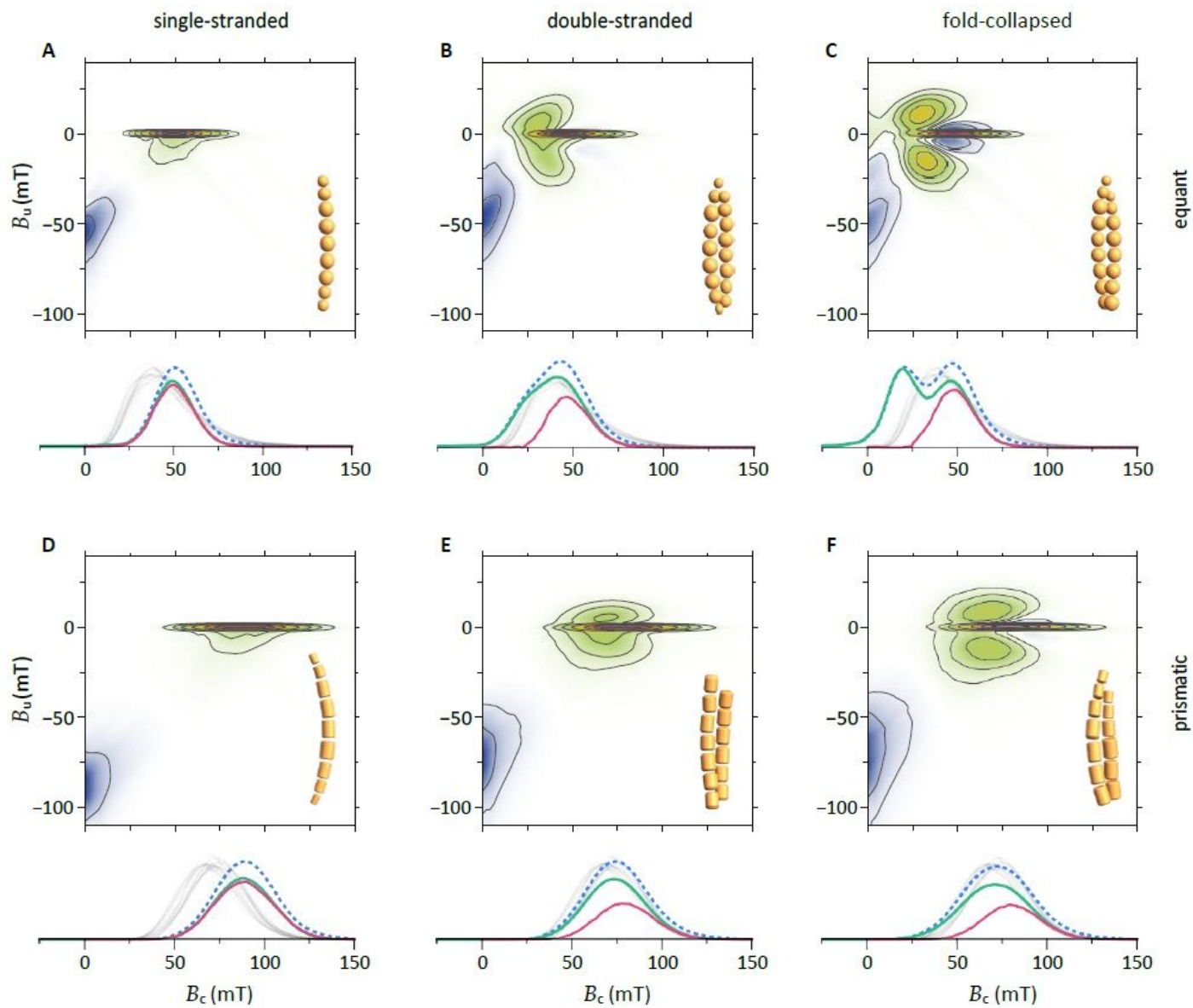


**Figure 3**

Electron microscopy images of wild-type and mutant AMB-1 cells.

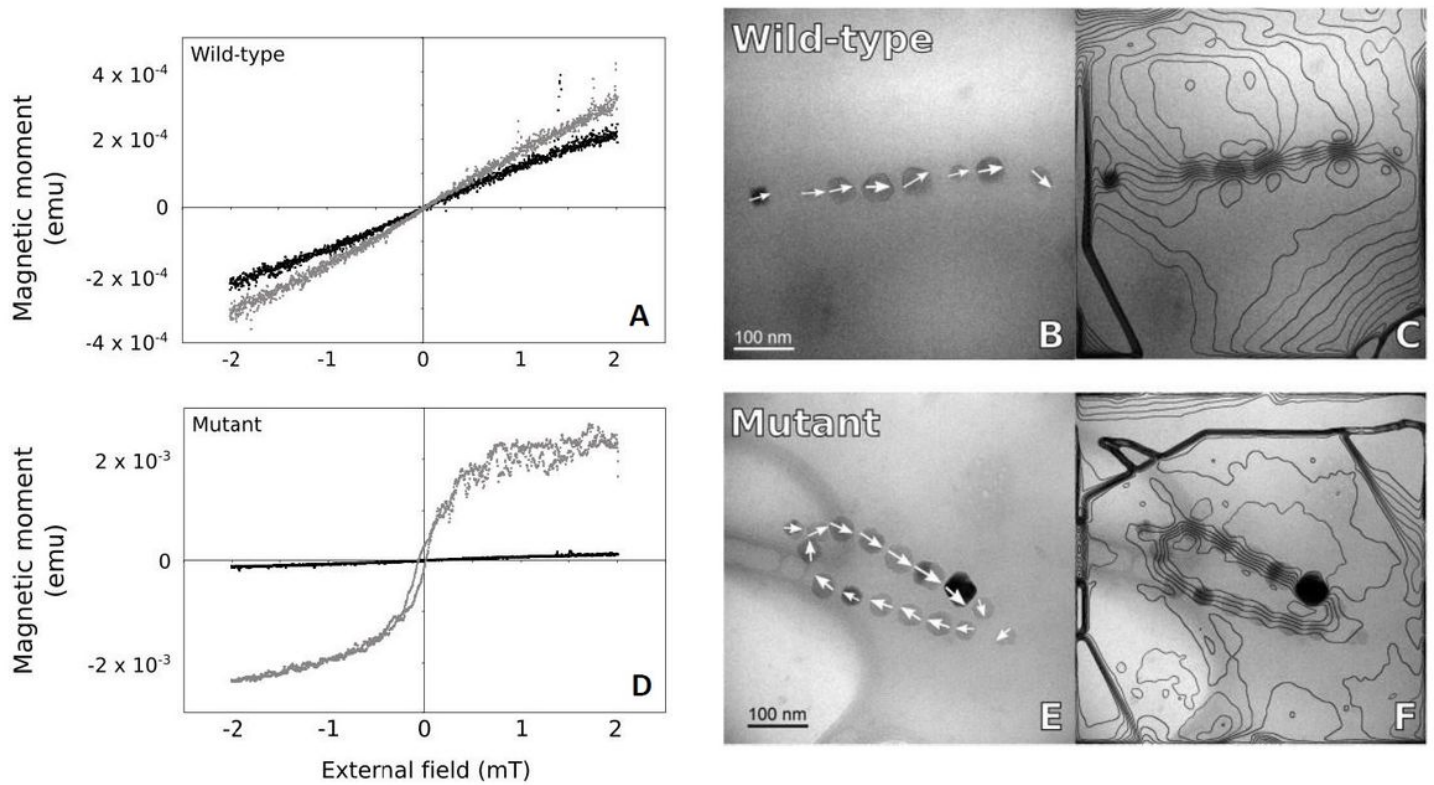


**Figure 4**

Native magnetic states of wild-type AMB-1 and the AMB-1 mutant. Magnetization of a suspension of (A) wild-type and (D) mutant AMB-1 cells in small fields varying between  $\pm 2$  mT, before (black) and after (gray) saturation in a 200 mT field. Electron microscopy and corresponding magnetic phase contours determined by off-axis electron holography images of (B-C) wild-type and (E-F) mutant magnetite chains.

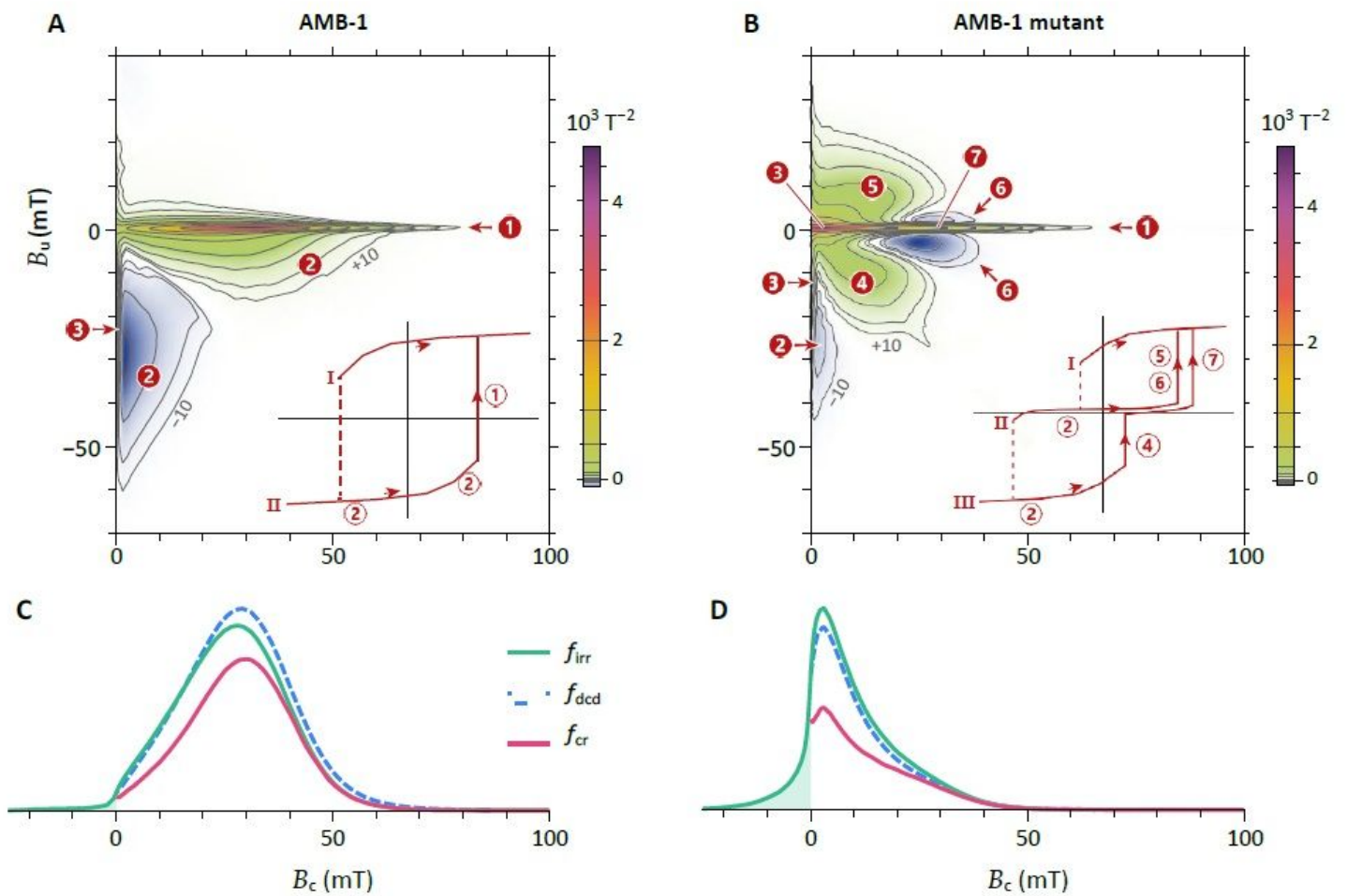


**Figure 5**

Magnetic properties of wild-type AMB-1 and the AMB-1 mutant. (A-B) FORC diagrams normalized by the saturation magnetization, with same logarithmically spaced contours. Insets are schematic representations of the magnetization of an individual cell as a function of the applied field. Numbers highlight the following features: 1 – central ridge created by the magnetization jump through which the lowest curve merges with curve I; 2 – positive and negative contributions from reversible magnetic moment rotation (difference between the slopes of consecutive curves); 3 – signatures of magnetically viscous particles (vertical ridge and central ridge extending to the origin); 4 – nucleation of a negative FC state from a negative SD state (contribution of the first magnetization jump in curve III to the difference between curves II and III); 5 – annihilation of a positive FC state (contribution of the magnetization jump in curve II to the difference between curves I and II); 6 – same as 5, but for the difference between curve II and III; 7 – annihilation of a negative FC state (contribution of the second magnetization jump in curve III to the difference between curves II and III). (C-D) Coercivity distributions of wild-type AMB-1 and the AMB-1 mutant, obtained from subsets of FORC data:  $f_{irr}$  – irreversible component of the ascending hysteresis branch,  $f_{dcd}$  – DC demagnetization of  $M_{rs}$ ,  $f_{cr}$  – central ridge. The shaded area represents the  $f_{irr}$  contribution of SD magnetic states that cannot exist in a null field.

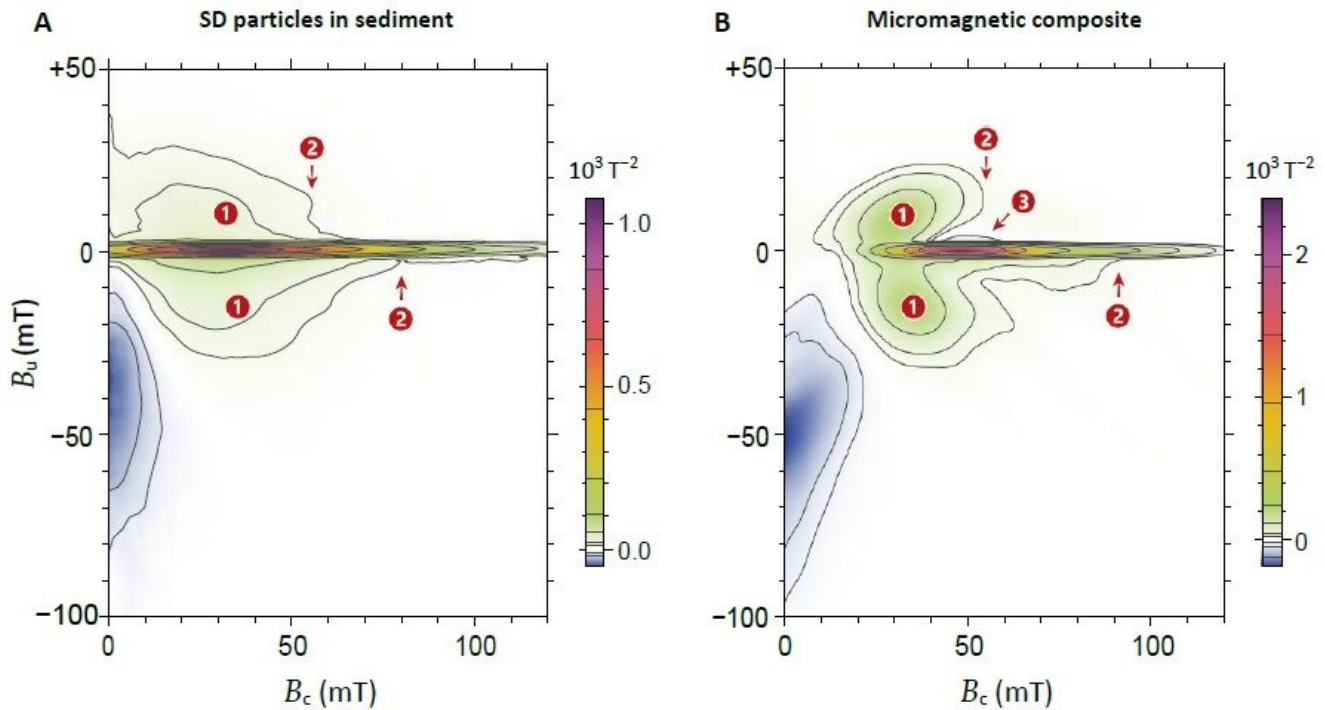


**Figure 6**

Comparison between the FORC signature of SD particles in a magnetofossil-rich sediment and synthetic results. (a) FORC diagram of in-situ  $<1\mu\text{m}$  magnetite particles (mostly SD) in a pelagic sediment [data from ref. 20]. (b) FORC diagram of a synthetic composite obtained from the six micromagnetically modelled chain structures, with the following relative contributions to the saturation magnetization, chosen for a visual match with (a): 21% (single-stranded chains of equant magnetosomes), 4% (single-stranded chains of prismatic magnetosomes), 42% (native double-stranded chains of equant magnetosomes), 8% (native double-stranded chains of prismatic magnetosomes), 21% (fold-collapsed chains of equant magnetosomes), 4% (fold-collapsed chains of prismatic magnetosomes). The same field range and contour levels with respect to the maximum amplitude are used in both plots to ease the comparison. Numbers highlight the following features: 1 – nucleation/annihilation of FC states, 2 – high-field limit of FC state nucleation/annihilation (asymmetric about the central ridge), 3 – residual negative amplitude from the annihilation of positive FC states, uncompensated by positive amplitudes from intermediate coercivity contributions.

## Supplementary Files

This is a list of supplementary files associated with this preprint. Click to download.

- [SIAppendix1.pdf](#)